A trimeric human angiotensin-converting enzyme 2 as an anti-SARS-CoV-2 agent

Tianshu Xiao[1,2], **Jianming Lu**[3,#], **Jun Zhang**[1,2,#], **Rebecca I. Johnson**[4,&], **Lindsay G.A. McKay**[4,&], **Nadia Storm**[4,&], **Christy L. Lavine**[5], **Hanqin Peng**[1], **Yongfei Cai**[1,2], **Sophia Rits-Volloch**[1], **Shen Lu**[3], **Brian D. Quinlan**[6], **Michael Farzan**[6], **Michael S. Seaman**[5], **Anthony Griffiths**[4], **Bing Chen**[1,2,*]

[1]Division of Molecular Medicine, Boston Children's Hospital, 3 Blackfan Street, Boston, MA 02115

[2]Department of Pediatrics, Harvard Medical School, 3 Blackfan Street, Boston, MA 02115

[3]Codex BioSolutions, Inc., 401 Professional Drive, Gaithersburg, MD 20879,

[4]Department of Microbiology, Boston University School of Medicine and National Emerging Infectious Diseases Laboratories, 620 Albany Street, Boston, MA 02118

[5]Center for Virology and Vaccine Research, Beth Israel Deaconess Medical Center, 330 Brookline Avenue, Boston, MA

[6]Department of Immunology and Microbiology, Scripps Research Institute, 130 Scripps Way, Jupiter, FL 33458

Abstract

Effective intervention strategies are urgently needed to control the COVID-19 pandemic. Human angiotensin-converting enzyme 2 (ACE2) is a membrane-bound carboxypeptidase that forms a dimer and serves as the cellular receptor for SARS−CoV−2. ACE2 is also a key negative regulator of the renin-angiotensin system (RAS) that modulates vascular functions. We report here the properties of a trimeric ACE2 ectodomain variant, engineered using a structure-based approach.

*Correspondence to: Bing Chen, phone: 617-355-4625, FAX: 617-730-1967, bchen@crystal.harvard.edu.
#These authors contributed equally to this work.
&These authors contributed equally to this work.

Competing Interests Statement:
Boston Children's Hospital has filed a patent application based on this work with B.C., T.X., J.Z. and Y.C. listed as co-inventors. All other authors declare no competing interests.

Data availability:
The atomic structure coordinates and EM maps are deposited in the wwPDB and EMDB, respectively, under the accession numbers PDB 7KJ2 and EMD-22891 (SARS-CoV-2 S in complex with one ACE2), PDB 7KJ3 and EMD-22892 (SARS-CoV-2 S in complex with two ACE2), PDB 7KJ4 and EMD-22893 (SARS-CoV-2 S in complex with three ACE2), PDB 7KJ5 and EMD-22894 (SARS-CoV-2 S, no ACE2). Source data are available with the paper online.

The trimeric ACE2 variant has a binding affinity of ~60 pM for the spike (S) protein of SARS−CoV−2 (compared to 77 nM for monomeric ACE2 and 12–22 nM for dimeric ACE2 constructs), while preserving its peptidase activity and the ability to block activation of angiotensin II receptor type 1 in the RAS. Moreover, the engineered ACE2 potently inhibits infection of SARS−CoV−2 in cell culture. These results suggest that engineered, trimeric ACE2 may be a promising anti-SARS-CoV-2 agent for treating COVID-19.

Introduction

The current COVID-19 pandemic, caused by severe acute respiratory syndrome coronavirus 2 (SARS−CoV−2), has infected more than 29 million people worldwide, leading to over 900 thousand deaths, with devastating socio-economic impacts. Effective intervention strategies are urgently needed to control the pandemic.

Since the outbreak of the virus, several therapeutic approaches have been evaluated in the hope of providing a viable treatment for COVID-19. First, convalescent sera from individuals recovered from the infection were used with encouraging results[1–3], but also some drawbacks (e.g., batch variations, possible blood-borne pathogens and blood-type matching). Second, patient-derived, potently neutralizing monoclonal antibodies have been isolated, which could provide a more powerful passive immunotherapy than convalescent sera[4–7]. Third, structure-guided design of peptide-based viral entry inhibitors has yielded promising leads in *in vitro* assays[8,9]; their efficacy requires further clinical evaluation. Fourth, known drugs or drug candidates, including remdesivir, favipiravir and ribavirin (viral RNA polymerase inhibitors); lopinavir and ritonavir (viral protease inhibitors); as well as hydroxychloroquine, corticosteroids and interferons (with more complicated antiviral mechanisms), have been repurposed as COVID-19 therapuetics[10,11]. Among them, remdesivir has received Emergency Use Authorizations (EUA) from the U.S. Food and Drug Administration (FDA), while hydroxychloroquine has been shown to be ineffective[12]. Finally, many new therapeutic candidates are in various stages of development (ref[13,14]; https://www.bio.org/policy/human-health/vaccines-biodefense/coronavirus/pipeline-tracker). While the infection resolves on its own in most asymptomatic and mild cases over time, COVID-19 in severe cases appears to progress in two phases – initial active viral replication in the respiratory system and subsequent excessive immune responses leading to multiple organ failure and possible death[15]. Thus, antivirals alone may be insufficient to change the course of disease progression for the population that needs intervention the most if administrated too late.

Human angiotensin-converting enzyme 2 (ACE2) is the cellular receptor for SARS-CoV-2 and binds the receptor binding domain (RBD) of the spike (S) protein of the virus to promote viral entry into the host cells and initiate infection[16,17]. The interactions between soluble ACE2 and SARS-CoV-2 RBD have been studied extensively within a very short period of time[18–20]. The intact ACE2 is a type I membrane glycoprotein containing an extracellular ectodomain that has metallopeptidase activity. Its neck domain near the transmembrane anchor mediates dimerization[20]. ACE2 is also a key negative regulator of the renin-angiotensin system (RAS) - a major hormone system, conserved in mammals and

some other vertebrate animals, for modulating vascular function[21,22]. The RAS controls extracellular fluid volume and blood pressure homeostasis by regulating the levels of renin and angiotensins in the circulation. Renin cleaves angiotensinogen to release angiotensin I (Ang I), which can be further processed by angiotensin-converting enzyme (ACE) into angiotensin II (Ang II) - a vasoconstrictive peptide that raises blood pressure and increases the extracellular fluid volume in the body by activating the angiotensin II receptors, including angiotensin II receptor type I (AT1R)[23]. ACE2 primarily converts Ang II to angiotensin-(1–7) (Ang 1–7), which is a vasodilator, thereby counter-balancing the effect of ACE/Ang II and playing critical roles in preventing hypertension and tissue damages[24].

The protective roles of ACE2 in acute respiratory distress syndrome (ARDS) and acute lung injury (ALI) have been demonstrated in animal models[25–27]. A recombinant soluble human ACE2 (rhACE2) was recently reported to block SARS-CoV-2 infection in cell culture and human organoids[28], prompting a phase 2 clinical trial for use of rhACE2 as a treatment for COVID-19 patients (NCT04335136). Thus, administration of exogenous ACE2 may be a promising therapeutic strategy for treating COVID-19, because it could not only block viral spread but also modulate the RAS to prevent organ injury. We therefore set out to design a series of ACE2 variants to enhance their binding affinity for SARS-CoV-2 S protein and their potency in blocking SARS-CoV-2 infection.

Results

Structures of soluble ACE2 in complex with SARS-CoV-2 S protein trimer

To facilitate design of ACE2-based viral fusion inhibitors, we first determined, by cryo-EM, the structures of a monomeric soluble ACE2 (residue 18–615) in complex with a stabilized soluble SARS-CoV-2 S protein trimer (Extended Data Fig. 1; ref[29]). We prepared the complex by mixing the two proteins because the monomeric ACE2 dissociates from S trimer very rapidly[30]. After 3D classification (Extended Data Figs. 2 and 3; Table 1), we found four distinct classes that represent S trimer with different number of ACE2 bound: no ACE2 (in the one-RBD-up conformation); and with one to three ACE2 bound (Fig. 1). Consistent with previous findings with ACE2 binding to SARS-CoV S protein as well as a recent SARS-CoV-2 study[31], ACE2 interacts with the RBD in its up conformation. While the NTD (N-terminal domain) of S1 shifts outwards slightly, the S2 portion remains largely unchanged upon ACE2 binding, even when compared to our recently published structure of the full-length S protein in the closed prefusion conformation[30]. The structure of the complex with three ACE2 bound is not symmetrical, as the distances between the C-termini of the three ACE2s (residue Tyr613) are 107Å, 109Å and 120Å, respectively (Extended Data Fig. 4). This distance in the complex with two ACE2s bound is 110Å. These observations suggest that there is a modest degree of freedom for the up conformation of RBD when ACE2 is bound. All the substrate binding sites of the bound ACE2s face away from the threefold axis of the S trimer (Extended Data Fig. 4), incompatible with the structure of the full length ACE2 dimer in complex with the amino acid transporter B^0AT1, in which the two active sites of the two protomers are facing each other[20]. If the B^0AT1-bound ACE2 dimer is indeed the form recognized by SARS-CoV-2, it appears that only one ACE2 protomer in the

dimer can bind one RBD in an S trimer unless there are unexpectedly large structural rearrangements in either ACE2 or S.

Design of ACE2 variants to enhance its binding affinity to SARS-CoV-2 S trimer

Measurements of the binding kinetics of soluble monomeric ACE2 ($ACE2_{615}$; Fig. 2) to the SARS-CoV-2 S trimer shows a relatively fast dissociation rate[30], limiting its ability to compete with the membrane bound ACE2 on the surface of a target cell. We therefore sought to enhance the effective affinity by creating a trimeric form of soluble ACE2. We fused a trimerization foldon tag, derived from bacteriophage T4 fibritin[32], to the C-terminal end of the ACE2 peptidase domain (residue 615) through a 11-residue flexible linker, a construct we refer to as $ACE2_{615}$-foldon (Fig. 2). We have also created another version ($ACE2_{615}$-LL-foldon) with a slightly longer linker (LL) with 13 residues between ACE2 and the foldon tag to assess its impact on binding. To further strengthen the interaction between ACE2 and the RBD, we introduced mutations guided by high-resolution structures (Extended Data Fig. 5; ref[18]), at three different positions in the ACE2-RBD interface, namely T27, H34 and K353. Substitution with a bulky hydrophobic residue at each of these sites may enhance hydrophobic interactions between the two proteins and slow the dissociation (Extended Data Fig. 5). We designed five mutants, T27Y, T27W, H34W, K353Y and K353W, in the $ACE2_{615}$-foldon background. Finally, for comparison, we also include two versions of dimeric forms, $ACE2m_{615}$-Fc and $ACE2_{740}$-Fc, both fused to an Fc domain of an immunoglobulin G (Fig. 2a). ACE2m615-Fc contains H374N and H378N mutations at its peptidase active site and ACE2740-Fc includes the neck domain that mediates dimerization in the full length ACE2[20].

To produce the soluble recombinant ACE2 and its variants, we transfected HEK293 cells with the expression constructs of the monomeric and trimeric forms containing a C-terminal his tag and purified the proteins by Ni-NTA and gel filtration chromatography. The two dimeric forms were purified by protein G resin followed by gel filtration chromatography. While the monomeric and dimeric forms of soluble ACE2 were mostly secreted into cell medium, as judged by western blot, the trimeric $ACE2_{615}$-foldon and its mutants were largely retained inside the cells. We therefore purified the secreted monomer and dimers from the cell supernatants and all the trimers from the cell lysates. Most proteins eluted from a size-exclusion column as a major symmetrical peak, regardless their secretion status (Extended Data Fig. 6). The $ACE2_{740}$-Fc protein containing the dimerizing neck domain appeared to aggregate substantially more than other constructs. The $ACE2_{615}$-foldon K353W mutant aggregated completely, and we therefore did not pursue this construct any further. Only the fractions from the major peak for each construct were pooled and used for subsequent analyses. We have also compared the secreted $ACE2_{615}$-foldon with the form purified from the cells and their biochemical properties are essentially identical (Extended Data Fig. 7).

Binding to SARS-CoV-2 soluble S trimer

We next measured binding of these recombinant ACE2 constructs to the stabilized soluble S trimer by bio-layer interferometry (BLI). As shown in Fig. 2b and Extended Data Fig. 8, the monomeric $ACE2_{615}$ had a fast dissociation rate and a K_D of 77 nM, consistent with the

measurement that we reported recently using surface plasmon resonance (SPR; ref[30]). The dimeric ACE2m$_{615}$-FC bound slightly more tightly (K$_D$ ~22 nM). The dimeric ACE2$_{740}$-Fc also bound more strongly than did the monomer (K$_D$ ~12 nM), although the dimer formed by the neck domain is not compatible with two ACE2 peptidase domains interacting with two distinct RBDs in a single S trimer (Extended Data Fig. 4). A possible explanation is that the neck domain mediated dimerization is not very strong and that the ACE2 peptidase domains are much more flexible than what the full-length ACE2 structure has indicated[20], particularly in the absence of B^{0}AT1. The trimeric ACE2$_{615}$-foldon interacted with the S trimer much more strongly than any of the monomeric or dimeric forms, with a K$_D$ of 1.2 nM. ACE2$_{615}$-LL-foldon with a longer linker between ACE2 and foldon showed an additional modest affinity enhancement (K$_D$ ~0.62 nM). The two interface mutants, ACE2$_{615}$-foldon-T27W and ACE2$_{615}$-foldon-T27Y, bound substantially more tightly than did the trimeric wild-type ACE2, with K$_D$s of ~60 and ~90 pM, respectively. While the H34W afforded a slight affinity increase, the K353Y mutation decreased affinity by more than 25-fold. Overall, these data show that our structure-guided design to increase the affinity of ACE2 to the S trimer, by trimerizing the receptor and by modifying the interface, has indeed been effective.

ACE2 peptidase activity and AT1R activation

We performed two independent assays to determine the enzymatic activity of these ACE2 constructs. First, we directly measured the peptidase activity using a synthetic peptide substrate that releases a free fluorophore upon ACE2 cleavage. In Fig. 3a, concentrations of all the proteins were normalized based on the number of active sites, and the fluorophore release was monitored continuously up to ~40 min. While all the trimeric forms showed essentially the same specific activity, the monomeric ACE2$_{615}$ and the dimeric ACE2$_{740}$-Fc had lower specific activities (Table 2 and Supplementary Table 1). The ACE2m$_{615}$-Fc was inactive due to the mutations at the active site. Thus, all these ACE2 constructs with the wildtype sequence at the active site retained their wildtype peptidase activity.

To further support this conclusion, we next tested the ability of the ACE2 constructs to block Ang II-induced activation of AT1R. In Fig. 3b, an Ang II peptide was first directly incubated with various ACE2 proteins and then added to HEK293 cells transfected with an AT1R expression construct. Activation of AT1R was monitored by changes in the intracellular calcium concentration. When the digestion reaction was quenched by EDTA at time 0 as a control, all the mixtures with different ACE2 proteins could efficiently activate AT1R, suggesting that nothing in our protein preparations inhibited Ang II-mediated AT1R activation. In contrast, when the digestion was allowed to proceed for 40 min, all AEC2 constructs except for the inactive ACE2m$_{615}$-Fc effectively blocked AT1R activation, presumably by converting Ang II to Ang 1–7, in agreement with the peptidase activity results.

Inhibition of SARS-CoV-2 infectivity in cell culture

We used three different assays to assess the neutralization potency of the ACE2 constructs in blocking SARS-CoV-2 infection. The circulating strain during the early days of the pandemic contained a D614 residue in its S protein, but it has subsequently been replaced by

an emerging strain harboring a G614 substitution[33]. It has been difficult to generate pseudotyped viruses with the full-length S from the D614 strain[34]. We first used an MLV-based pseudovirus assay with a D614 S construct lacking 19 residues of the cytoplasmic tail, which incorporates efficiently into pseudoviruses. In Fig. 4a, the monomeric $ACE2_{615}$ showed the lowest potency with an IC_{50} value of 24.1 μg/ml. The two dimeric forms, $ACE2m_{615}$-Fc and $ACE2_{740}$-Fc, and the trimeric mutant $ACE2_{615}$-foldon-K353Y had greater potency, with IC_{50} values ranging from 1.2 to 6.3 μg/ml. The two trimeric forms, $ACE2_{615}$-foldon and $ACE2_{615}$-LL-foldon, and the trimeric mutant $ACE2_{615}$-foldon-H34W neutralized with even greater potency and an IC_{50} value around 0.6 μg/ml. The most potent inhibitors were $ACE2_{615}$-foldon-T27W and $ACE2_{615}$-foldon-T27Y, which had IC_{50} values of 0.21 and 0.25 μg/ml, respectively. Thus, the neutralization potency of these ACE2 constructs correlates strictly with their binding affinity, suggesting that the interaction between ACE2 and S is the principal determinant of neutralization of the virus pseudotyped with the CT-truncated S (D614). Neutralization by these ACE2 proteins in the HIV-based pseudovirus assay using a full-length S derived from the G614 circulating strain showed a very similar pattern with $ACE2_{615}$ the weakest and $ACE2_{615}$-foldon-T27W and $ACE2_{615}$-foldon-T27Y the most potent (Fig. 4b). Furthermore, when they were analyzed by a plaque assay with an authentic SARS-CoV-2 (Fig. 4c), the neutralization pattern was almost identical to that from the MLV-based assay (Table 2 and Supplementary Table 2). The IC_{50} values for $ACE2_{615}$-foldon-T27W and $ACE2_{615}$-foldon-T27Y were 0.08 and 0.14 μg/ml, respectively. These results indicate that the engineered ACE2 constructs are very potent agents for blocking SARS-CoV-2 infection in cell culture.

Discussion

A recombinant human ACE2, named APN01, is currently under evaluation as a treatment for COVID-19 in a phase 2 clinical trial (NCT04335136), primarily based on the favorable results from a previous phase 1 safety and tolerability trial (NCT00886353) in a small number of healthy individuals[35], as well as on the recent evidence that the protein blocks SARS-CoV-2 infection effectively *in vitro*[28]. APN01 is a soluble ACE2 construct expressing residues 1–740 and probably dimerizes by the neck domain[36], like $ACE2_{740}$-Fc used in our study. We demonstrate here that our best trimeric ACE2 variant, $ACE2_{615}$-foldon-T27W, has >200-fold higher binding affinity for the soluble SARS-CoV-2 S trimer, and ~5-fold and ~13-fold higher neutralization potency against pseudoviruses and authentic viruses, respectively, than does $ACE2_{740}$-Fc, while its peptidase activity and ability to block AT1R activation remain essentially unchanged.

Using a deep mutagenesis screening approach, a recent study has identified a dimeric ACE2 variant containing multiple mutations, which led to higher affinity binding to the RBD, but also a substantial loss in the catalytic activity (4–8 fold decrease) than the parental construct with the wildtype sequence[37]. One of the mutations from the mutagenesis screening is T27Y, coinciding with our structure-based design. Another study reported a trimeric ACE2 construct with the wildtype sequence[38], similar to our $ACE2_{615}$-foldon protein. Moreover, *de novo* protein design based on the ACE2 helix that interacts with the RBD without the catalytic domain has led to picomolar SARS-CoV-2 miniprotein inhibitors[39]. Our approach,

however, distinguishes the S protein binding and the peptidase activity, which can be manipulated separately to maximize the therapeutic benefits of an ACE2 construct.

Although the molecular mechanism by which a soluble ACE2 blocks SARS-CoV-2 infection as a decoy receptor is obvious, its protective role against lung injury – a hallmark of severe COVID-19 cases – appears to be more complicated in humans than in animal models. ACE2 knockout mice have more severe ARDS symptoms than do wildtype mice, whereas ACE2 overexpression appears to be protective[25]. Moreover, administration of recombinant ACE2 reduces severity of lung injury in mice caused by respiratory syncytial virus or influenza virus[26,27]. In humans, rhACE2 was well tolerated with a short half-life[35], but its infusion did not appear to ameliorate ARDS at least in a small number of patients[40]. A recent case report described using APN01 to treat a severe COVID-19 patient with a very encouraging outcome[41]. The ongoing phase 2 clinical trial with expected 200 participants may provide much needed information regarding the therapeutic potential of recombinant ACE2 in the context of COVID-19. Structure-based modifications presented here may help augment therapeutic efficacy while suppressing adverse effects, if any.

The safety in humans of the foldon trimerization tag, derived from the bacteriophage T4 fibritin[32], has been demonstrated by vaccine trials against HIV-1 and SARS-CoV-2 in clinical settings[42,43]. However, a dose in mg/kg body weight of the trimeric ACE2 proteins as a therapeutics is likely much greater than that used as a vaccine (for example, 50–250 μg of foldon stabilized HIV-1 gp140 protein/injection; ref[42]). If the foldon tag induces unacceptable levels of side effects at a high dose in animals or humans, other trimerization domains, such as those in abundant human collagens[44], can be considered. Further improvements of these ACE2-based therapeutic candidates include modifications to enhance protein stability by introducing additional disulfide bonds (which may reduce the catalytic activity), to modulate peptidase activity by mutating residues in or near the active site, and to increase its in vivo residence time in circulation, by strategies such as PEGylation[45].

The structure of the membrane-bound ACE2 dimer formed by the neck domain is not compatible with a binding mode of two protomers interacting with two RBDs from a single S trimer, as depicted in Extended Data Fig. 4. Much stronger binding of $ACE2_{740}$-Fc to the S trimer, as well as greater neutralization potency than those of monomeric $ACE2_{615}$ and even dimeric $ACE2m_{615}$-Fc clearly indicate avidity, suggesting that the ectodomain of either ACE2 or SARS-CoV-2 S protein has much greater flexibility than the cryo-EM structures imply[20,30,46,47]. If the multivalency of the trimeric S protein on the surface of virion and the dimeric ACE2 on the host cells indeed plays an important role during viral attachment, the binding affinity for the virus to latch on the target cells would be much stronger than the values measured using monomeric ACE2[46]. It may help explain the unexpected transmission efficiency of SARS-CoV-2 leading to a pandemic on a surprising scale and raise the hurdle for antivirals to effectively compete with ACE2 for S binding. Trimeric ACE2 variants exerting even greater avidity than the dimeric form on the host cells may have a competitive edge over other RBD-targeting inhibitors, such as monoclonal antibodies, with similar binding affinity.

Online methods

Cell lines

HEK 293T cells were purchased from ATCC; Expi293F from Thermo Fisher Scientific. Mycoplasma contamination has been routinely tested for cell culture in our laboratory.

Protein expression and purification

A synthetic gene encoding an human ACE2 fragment (residues 1–615) fused with a C-terminal 6xHis tag was generated by GenScript (Piscataway, NJ) and cloned into pCMV-IRES-puro expression vector (Codex BioSolutions, Inc, Gaithersburg, MD) to create the construct pACE2$_{615}$. To construct a trimeric ACE2 variant, a DNA fragment encoding a foldon trimerization tag was inserted between the ACE2 fragment and the His tag by restriction digestion and DNA ligation to give the plasmid pACE2$_{615}$-foldon. Site-specific mutations, guided by high-resolution crystal structures (Extended Data Fig. 5), were introduced to the ACE2$_{615}$-foldon construct by PCR following standard protocols of site-directed mutagenesis. All the ACE2 variants were expressed in HEK 293F cells by transient transfection using Opti-MEM (Gibco-Thermo Fisher Scientific, Waltham, MA). After incubation for 4 days at 37°C with 5.5% CO_2, the transfected cells were harvested by centrifugation at 2,524 xg for 30 minutes.

For the monomeric ACE2$_{615}$ protein, the cell supernatant was collected by centrifugation and loaded onto a column packed with Ni-NTA agarose beads (Qiagen, Hilden, Germany). The column was washed with a buffer containing 20 mM Tris-HCl, pH 7.5, and 300 mM NaCl. The protein was eluted using a buffer containing 100 mM imidazole, and further purified by gel filtration chromatography on a Superdex 200 Increase 10/300 GL column (GE Healthcare, Chicago, IL)

To purify the dimeric ACE2$_{615}$-Fc and ACE2$_{740}$-Fc proteins, the cell supernatant was collected and loaded to a column packed with GammaBind Plus Sepharose beads (GE Healthcare). The column was washed with PBS. The protein was eluted using 100 mM glycine (pH 2.5) and neutralized immediately with 2 M Tris-HCl (pH 8.0). The eluted protein was further purified by gel filtration chromatography on a Superdex 200 Increase 10/300 GL column.

For all the ACE2$_{615}$-foldon variants, which were not secreted efficiently, the cell pellet was resuspended in the lysis buffer (20 mM Tris-HCl, pH 7.5, 300 mM NaCl, 1% NP40, 20 mM imidazole) and rocked gently for 1 hour at 4°C, followed by spinning at 17,554 xg for 30 minutes to remove cell debris. The supernatant was loaded to a column packed with Ni-NTA agarose beads (Qiagen). The column was washed with a buffer containing 20 mM Tris-HCl, pH 7.5, 300 mM NaCl and 50 mM imidazole and the protein was eluted using a buffer containing 20 mM Tris-HCl, pH 7.5, 300 mM NaCl and 300 mM imidazole. The eluted protein was further purified by gel filtration chromatography on a Superdex 200 Increase 10/300 GL column.

To produce a stabilized ectodomain of SARS-CoV-2 S trimer protein, a synthetic gene (kindly provided by Dr. Dan Barouch), encoding residues 1–1208 with the furin cleavage

site (residues 682–685) replaced by a "GGSG" sequence, residues K986 and V987 substituted by prolines, and addition of a foldon trimerization tag followed by a C-terminal 6xHisTag, was cloned into the vector pCMV-IRES-puro. The expression construct was transiently transfected in HEK 293T cells using polyethylenimine (Polysciences, Inc, Warrington, PA). Protein was purified from cell supernatants using Ni-NTA resin (Qiagen), the eluted fractions containing S protein were pooled, concentrated, and further purified by gel filtration chromatography on a Superose 6 column (GE Healthcare).

Cryo-EM sample preparation and data collection

To prepare cryo grids, 3.5 μl of the freshly prepared mixture of the soluble S trimer and monomeric ACE2 (1:3 molar ratio) at ~1 mg/ml was applied to a 1.2/1.3 Quantifoil grid (Quantifoil Micro Tools GmbH, Germany), which had been glow discharged with a PELCO easiGlow™ Glow Discharge Cleaning system (Ted Pella, Inc., Redding, CA) for 60 s at 15 mA. Grids were immediately plunge-frozen in liquid ethane using a Vitrobot Mark IV (Thermo Fisher Scientific), and excess protein was blotted away using grade 595 filter paper (Ted Pella, Inc.) with a blotting time of 4 s, a blotting force of −12 at 4°C in 100% humidity. The grids were first screened for ice thickness and particle distribution using a Talos Arctica transmission electron microscope (Thermo Fisher Scientific), operated at 200 keV and equipped with a K3 direct electron detector (Gatan), at the Harvard Cryo-EM Center for Structural Biology. For data collection, images were acquired with selected grids using a Titan Krios transmission electron microscope (Thermo Fisher Scientific) operated at 300 keV with a BioQuantum GIF/K3 direct electron detector. Automated data collection was carried out using SerialEM version65 at a nominal magnification of 105,000× and the K3 detector in counting mode (calibrated pixel size, 0.825 Å) at a exposure rate of ~14.8 electrons per physical pixel per second. Each movie had a total accumulated electron exposure of 50 e/Å2 fractionated in 50 frames of 50 ms. Datasets were acquired using a defocus range of 1.5–2.6 μm.

Image processing, 3D reconstructions and model building

Drift correction for cryo-EM images was performed using MotionCor2[48], and contrast transfer function (CTF) was estimated by CTFFIND4[49] using motion-corrected sums without dose-weighting. Motion corrected sums with dose-weighting were used for all image processing. CrYOLO[50] was used for particle picking, and RELION3.0.8[51] was used for 2D classification, 3D classification and refinement. A total of 407,761 particles were extracted from 4,292 images. The selected particles were subjected to 2D classification, giving a total of 261,799 good particles. A low-resolution negative-stain reconstruction of the sample was low-pass-filtered to 40Å and used as an initial model for 3D classification in *C*1 symmetry. One class containing 32,685 particles appeared to represent the free S trimer with no ACE bound was further refined in C1 symmetry, giving a reconstruction at 3.6Å resolution. Another major class with ~49% of the selected particles showing density for ACE2 was refined in C1 symmetry and subsequently subjected to CTF refinement, Bayesian polishing and particle subtraction by masking out the ACE2-RBD density, followed by 3D classification without alignment in six classes. Whole particles were re-extracted based on the six classes from the masked local classification and refined further, revealing different stoichiometry for ACE2 binding (one ACE2 per S trimer, two ACE2 per S trimer, and three

ACE2 per S trimer). Three best maps representing each type of complexes were chosen and further refined in C1 symmetry after CTF refinement and Bayesian polishing, leading to one reconstruction of the complex with one ACE2 bound at 3.6Å resolution from 15,964 particles; another reconstruction of the complex with two ACE2 bound at 3.7Å resolution from 13,515 particles and a third reconstruction of the complex with three ACE2 bound at 3.4Å resolution from 26,298 particles. Reported resolutions are based on the gold-standard Fourier shell correlation (FSC) using the 0.143 criterion. All density maps were corrected from the modulation transfer function of the K3 detector and then sharpened by applying a temperature factor that was estimated using post-processing in RELION. Local resolution was determined using RELION with half-reconstructions as input maps.

The initial templates for model building used the stabilized SARS-CoV-2 S ectodomain trimer structure (PDB 6VYB) and ACE2 from the ACE2-B0AT1 complex structure (PDB 6M17). Several rounds of manual building were performed in Coot[52]. Iteratively, refinement was performed in both Phenix[53] (real space refinement) and ISOLDE[54], and the Phenix refinement strategy included rigid body fit, minimization_global, local_grid_search, and adp, with rotamer, Ramachandran, and reference-model restraints, using PDB 6VYB and PDB 6M17 as the reference model. The refinement statistics are summarized in Table 1. Structural biology applications used in this project were compiled and configured by SBGrid[55].

Binding assay by bio-layer interferometry (BLI)

Binding of ACE2 variants to the soluble S trimer was measured using an Octet RED384 system (ForteBio, Fremont, CA). Each ACE2 protein was diluted using the running buffer (PBS, 0.005% Tween 20, 0.25 mg/ml BSA) and transferred to a 96-well plate. The soluble S protein was immobilized to Amine Reactive 2nd Generation (AR2G) biosensors (Fortebio), following a protocol recommended by the manufacturer. After equilibrating in the running buffer for 5 minutes, the sensors with immobilized S protein were dipped in the wells containing the ACE2 protein at various concentrations (1.852–150 nM for $ACE2_{615}$; 0.926–75 nM for $ACE2_{615}$-Fc and $ACE2_{740}$-Fc; 0.617–50 nM for all the $ACE2_{615}$-foldon variants) for 5 minutes to measure the association rate. The sensors were then dipped in the running buffer for 10 minutes to determine the dissociation rate. Control sensors with no S protein were also dipped in the ACE2 solutions and the running buffer as references. Recorded sensorgrams with background subtracted from the references were analyzed using the software Octet Data Analysis HT Version 11.1 (Fortebio). The curves for monomeric ACE2 were fit to a 1:1 binding model, while those for the oligomeric ACE2 variants were fit to a bivalent binding model.

ACE2 peptidase activity assay

The catalytic activity of the ACE2 variants was measured by detecting a free fluorophore 7-methoxycoumarin-4-acetic acid (MCA) released from a synthetic peptide substrate, using an ACE2 activity kit (BioVision, Milpitas, CA). The $ACE2_{615}$ and $ACE2_{615}$-foldon variants were diluted to 0.25 μg/ml using the assay buffer from the kit. The $ACE2_{615}$-Fc and $ACE2_{740}$-Fc proteins were diluted to 0.38 and 0.30 μg/ml, respectively, to keep the same number of the active sites as other ACE2 variants. 50 μl of diluted protein was set in the 96-

well plate. Immediately before recording fluorescence signals, 50 µl substrate diluted in the assay buffer, following a protocol recommended by the manufacturer, was added to each well. Fluorescence signals were recorded in a kinetic mode by a Flexstation 3 Multi Mode Microplate Reader (Molecular Devices, San Jose, CA). The specific activity was calculated as the amount of the released fluorophore divided by the reaction time and the amount of the ACE2 protein using the data within the initial linear phase, as described in the protocol provided by the manufacturer. To determine the initial linear phase, fluorescence signals were recorded with 1.25, 0.25 and 0.125 µg of $ACE2_{615}$ protein, respectively, reaching maximum after the substrates were completely cleaved. Data from the first 2 minutes within the linear phase with signals less than 10% of the maximum were used for the calculation. The amount of released MCA was derived from the increase of the fluorescence signal divided by the slope of the MCA standard curve.

Inhibition of Ang II-induced AT1R activation

To treat the Ang II peptide with each ACE2 variant, 2 µl of ACE2 protein at 0.5 mg/ml were added to 198 µl of an assay buffer (1xPBS, 40 mM Tris-HCl, pH6.8, 20 µM $ZnCl_2$) containing 65 µM Ang II peptide. The reactions were incubated at 37°C for 40 min, and then quenched by addition of 50 µl of 0.5 M EDTA. The final concentration of Ang II peptide was 52 µM. As a time 0 control, 198 µl of the assay buffer containing 65 µM Ang II was incubated with EDTA at 37°C first, followed by addition of 2 µl of each ACE2 protein (0.5 mg/ml).

Changes in the intracellular calcium concentration in AT1R-expressing cells when induced by Ang II peptide were measured to monitor the activation of the receptor. Briefly, HEK293 cells were transfected with pCMV-AT1R-IRES-Puro gene using Lipofectamine 3000 reagent (Thermo Fisher Scientifics). Approximately 24 hours posttransfection, the cells were transferred into a 384-well black clear plate at a density of 1.2×10^4 cells/well in 20 µl culture medium. On day 4, 20 µl of 1x Non-Wash Calcium Dye solution (CB-80500–301, Codex BioSolutions Inc) was added into each well. The cell plate was incubated at 37°C in a CO_2 incubator for 1 hour. The pretreated ligands (Ang II peptide) at various concentrations (0.005–500 nM) were prepared in 1X HBSS with 20 mM HEPES (pH7.46). Fluorescent intensity in each well was recorded on an FDSS 7000 (Hamamatsu Corporation, Bridgewater, NJ) at the rate of 1 image/sec (Ex 480 nM and Em 540 nM) and the base line of each well was also recorded for 10 seconds. After the online addition of 10 µl of the prepared ligands (the final concentration of 0.001–100 nM), the fluorescent intensity of each well was recorded at the rate of 1 image/sec for additional 170 seconds.

MLV-based pseudovirus assay

Murine Leukemia Virus (MLV) particles (all plasmids of the MLV components were kindly provided by Dr. Gary Whittaker at Cornell University and Drs. Catherine Chen and Wei Zheng at National Center for Advancing Translational Sciences, National Institutes of Health), pseudotyped with a SARS-CoV-2 S protein construct were generated in HEK 293T cells, following a protocol described previously for SARS-CoV[56,57]. To enhance incorporation, C-terminal 19 residues in the cytoplasmic tail of the SARS-CoV-2 S protein containing D614 were deleted. To prepare for infection, 7.5×10^3 of Expi-293F cells, stably

transfected with a full-length human ACE2 expression construct, in 15 μl culture medium were plated into a 384-well white-clear plate coated with poly-D-Lysine to enhance cell attachment. On day 2, 12.5 μl of SARS-CoV-2 MLV pseudoviruses were mixed with 5 μl of each ACE2 variant at different concentrations (0.001–300 μg/ml) and incubated at 37°C for 1 hr. After the medium in each well containing the cells was removed, 17.5 μl of each ACE2-virus mixture were added. The plate was centrifuged at 54 xg for 15 min at 4°C and additional 7.5 μl of culture medium were then added. The total final volume in each well was 25 μl. The cells were then incubated at 37°C for 42 hr. Luciferase activities were measured with Firefly Luciferase Assay Kit (CB-80552–010, Codex BioSolutions Inc). IC_{50} values were calculated based on curve fitting in GraphPad Prism.

HIV-based pseudovirus assay

Neutralization of HIV-based pseudovirus containing a full-length SARS-CoV-2 S protein was measured using a single-round infection assay in HEK 293T/ACE2 target cells. Pseudotyped virus particles were produced in 293T/17 cells (ATCC) by co-transfection of a plasmid encoding codon-optimized SARS-CoV-2 full-length S containing G614, a packaging plasmid pCMV R8.2 expressing HIV gag and pol, and a luciferase reporter plasmid pHR' CMV-Luc. All plasmids were kindly provided by Dr. Barney Graham (NIH, Vaccine Research Center). The 293T cell line stably overexpressing the human ACE2 protein was created by the Farzan group at Scripps Research Institute. For neutralization assays, serial dilutions of the ACE2 constructs were performed in duplicate followed by addition of pseudoviruses. Plates were incubated for 1 hour at 37°C followed by addition of 293T/ACE2 target cells ($1×10^4$/well). Wells containing cells and pseudoviruses without ACE2 proteins or cells alone were positive and negative infection controls, respectively. Assays were harvested on day 3 using BrightGlo luciferase reagent (Promega, Madison, WI) and luminescence detected with a Victor luminometer (PerkinElmer, Waltham, MA). IC_{50} values are reported as the ACE2 protein concentration that inhibited 50% virus infection. All neutralization experiments were repeated twice with similar results.

Neutralization of authentic SARS-CoV-2

ACE2 variants were serially diluted in Dulbecco's Phosphate Buffered Saline (DPBS) (Gibco™) using half-log dilutions starting at 31,579 ng/ml. Dilutions were prepared in triplicate for each protein. Each dilution was incubated at 37°C in 5% CO_2 for 1 hour with 1,000 plaque forming units/ml (PFU/ml) of SARS-CoV-2 (isolate USA‑WA1/2020). Controls included Dulbecco's Modified Eagle Medium (DMEM) (Gibco-Thermo Fisher Scientific) containing 2% fetal bovine serum (Gibco-Thermo Fisher Scientific) and antibiotic-antimycotic (Gibco-Thermo Fisher Scientific) only as a negative control, 1000 PFU/ml SARS-CoV-2 (USA-WA1/2020) incubated with DPBS, and 1000 PFU/ml SARS-CoV-2 incubated with DMEM. 200 μl of each dilution or control were added to confluent monolayers of NR-596 Vero E6 cells in triplicate and incubated for 1 hour at 37°C and 5% CO_2. The plates were gently rocked every 5–10 minutes to prevent monolayer drying. The monolayers were then overlaid with a 1:1 mixture of 2.5% Avicel® RC-591 microcrystalline cellulose and carboxymethylcellulose sodium (DuPont Nutrition & Biosciences, Wilmington, DE) and 2X Modified Eagle Medium (Temin's modification, Gibco-Thermo Fisher Scientific) supplemented with 2X antibiotic‑antimycotic, 2X GlutaMAX (Gibco-

Thermo Fisher Scientific) and 10% fetal bovine serum. Plates were incubated at 37°C and 5% CO_2 for 2 days. The monolayers were fixed with 10% neutral buffered formalin and stained with 0.2% aqueous Gentian Violet (RICCA Chemicals, Arlington, TX) in 10% neutral buffered formalin for 30 min, followed by rinsing and plaque counting. The half maximal inhibitory concentrations (IC_{50}) were calculated using GraphPad Prism 8.

Further information on experimental design is available in the Nature Research Reporting Summary linked to this article.

Extended Data
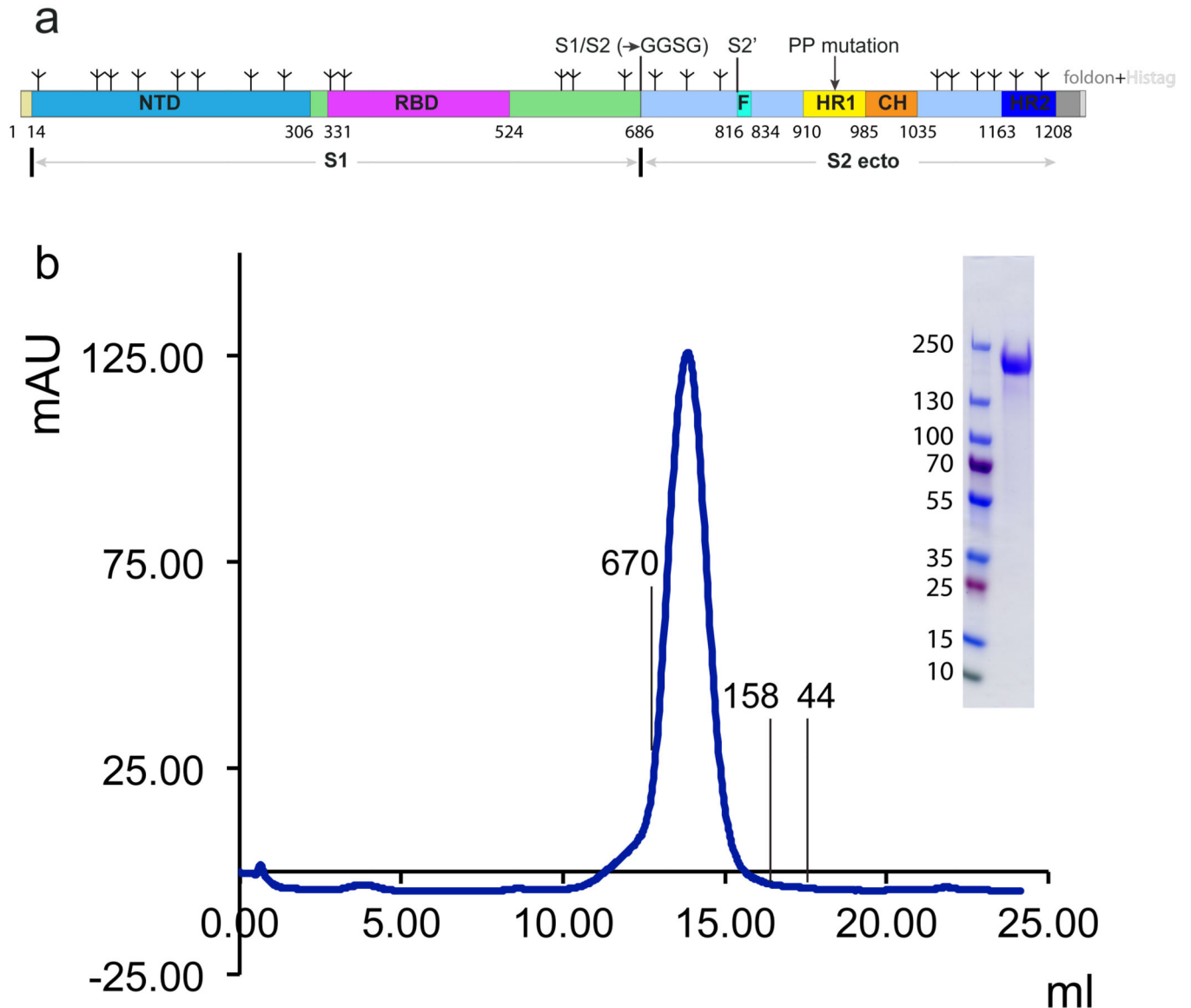
Extended Data Figure 1. Preparation of a stabilized soluble SARS-CoV-2 S trimer.
(a) Schematic representation of the expression construct of the soluble SARS-CoV-2 S protein. Segments of S1 and S2 ectodomain (S2ecto) include: NTD, N-terminal domain;

RBD, receptor-binding domain; S1/S2, S1/S2 cleavage site; S2', S2' cleavage site; FP, fusion peptide; HR1, heptad repeat 1; CH, central helix region; HR2, heptad repeat 2; and tree-like symbols for glycans. The S1/S2 cleavage site (RRAR) was mutated to GGSG. Two mutations K986P and V987P were introduced and a trimerization tag –foldon fused to the C-terminal end to stabilize the prefusion conformation[29]. A C-terminal histag was included for protein purification. (b) The purified S protein was resolved by gel-filtration chromatography on a Superose 6 column and the pooled peak fractions were analyzed by Coomassie stained SDS-PAGE. The molecular weight standards include thyoglobulin (670 kDa), γ-globulin (158 kDa) and ovalbumin (44 kDa). The uncropped image for panel b is available as source data.
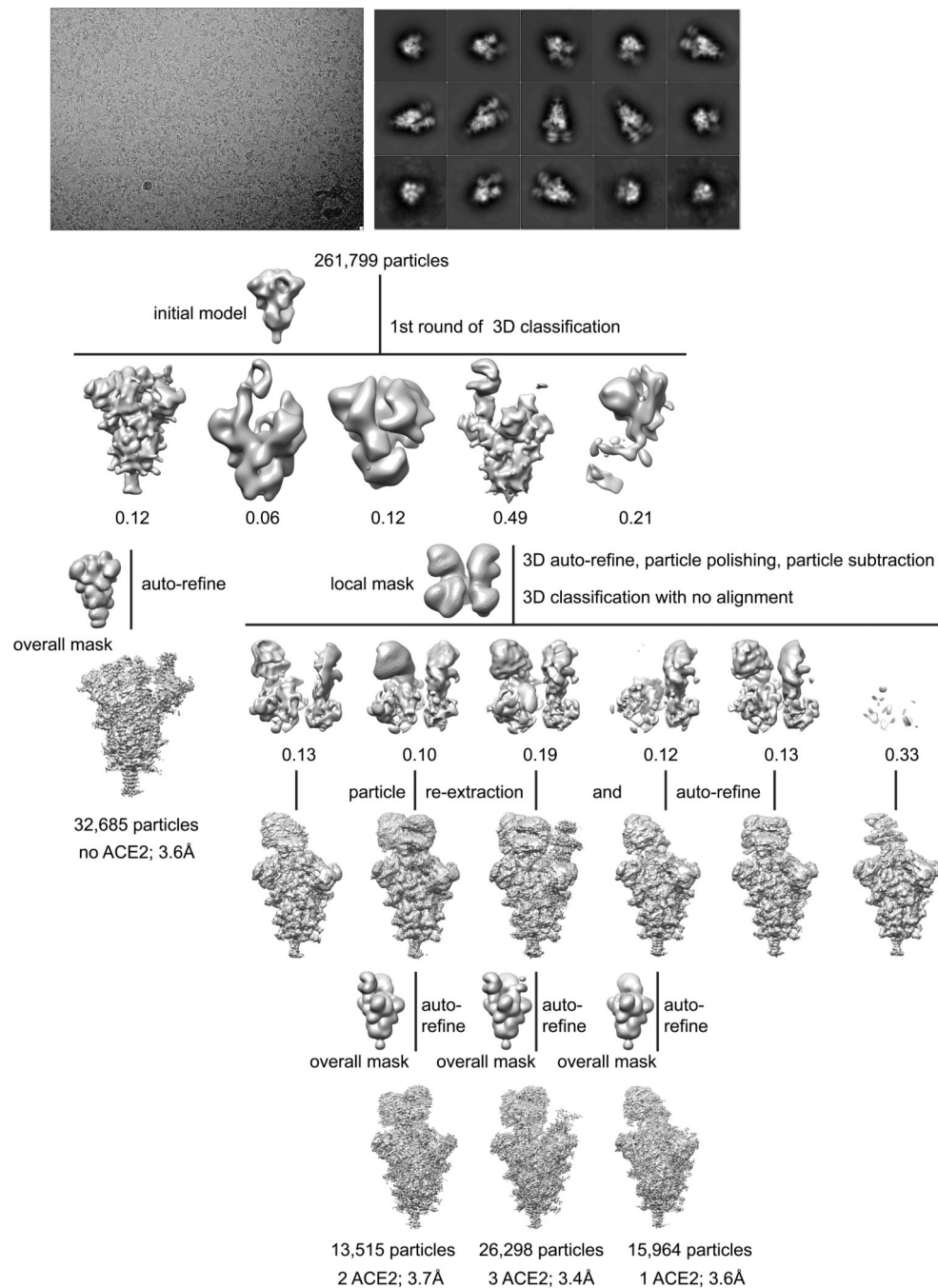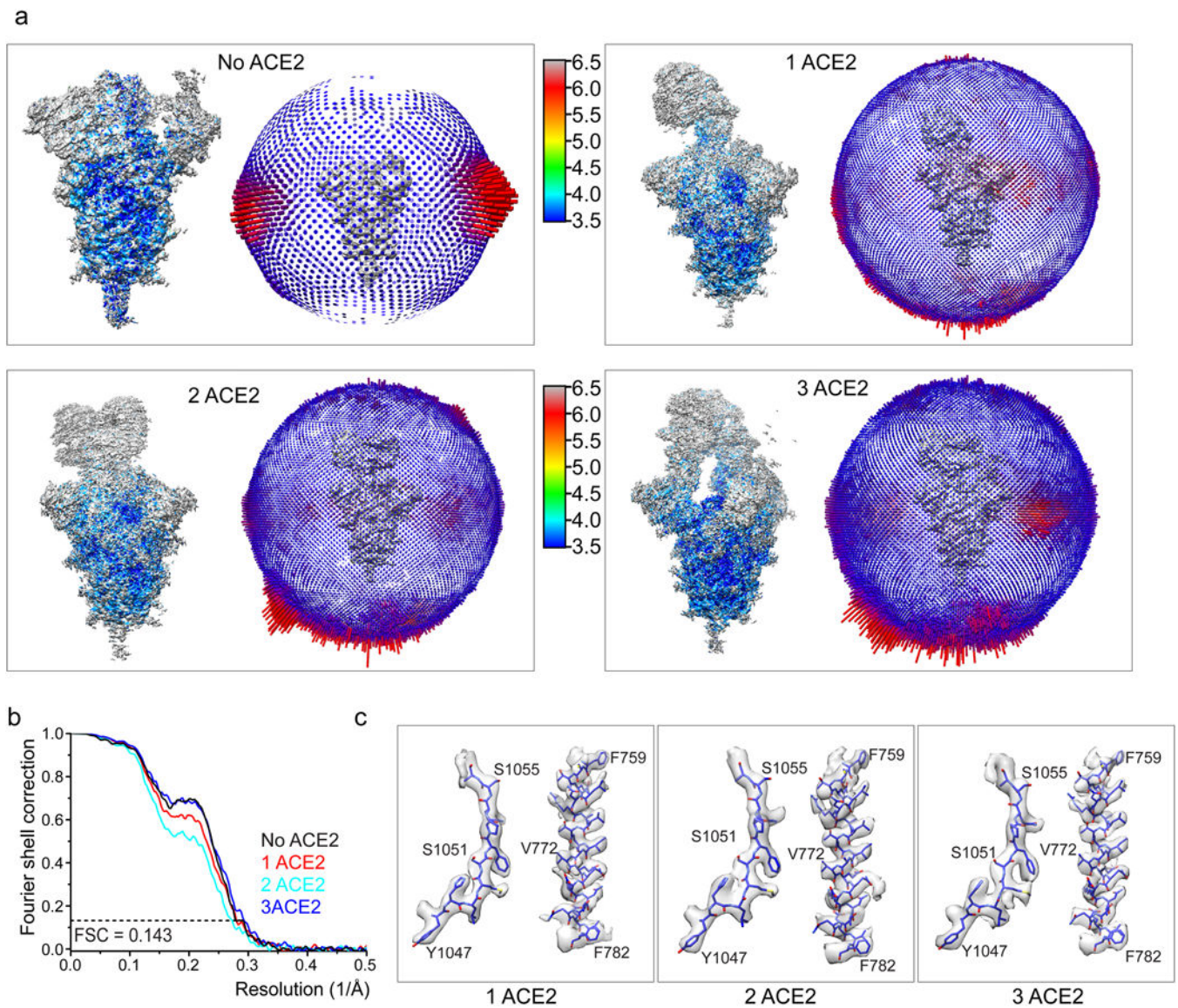
Extended Data Figure 2. Cryo-EM analysis of the ACE2-S complexes.
Top, representative micrograph, and 2D averages of the cryo-EM particle images showing secondary structural features. Bottom, data processing workflow for structures of the free S trimer (no ACE2), S trimer with one ACE2 bound (1 ACE2), S trimer with two ACE2 bound (2 ACE2), S trimer with three ACE2 bound (3 ACE2), as indicated.

Extended Data Figure 3. Analysis of the 3D reconstructions of the S-ACE2 complexes.
(a) 3D reconstructions of the S trimer and its ACE2 complexes are colored according to local resolution estimated by RELION. Angular distribution of the cryo-EM particles used in the reconstruction is shown in the side view of the EM map. (b) Gold standard FSC curves of the refined 3D reconstructions. (c) Representative density in gray surface from the EM maps. No ACE2), the free S trimer; 1 ACE2, S trimer with one ACE2 bound; 2 ACE2, S trimer with two ACE2 bound; 3 ACE2, S trimer with three ACE2 bound.
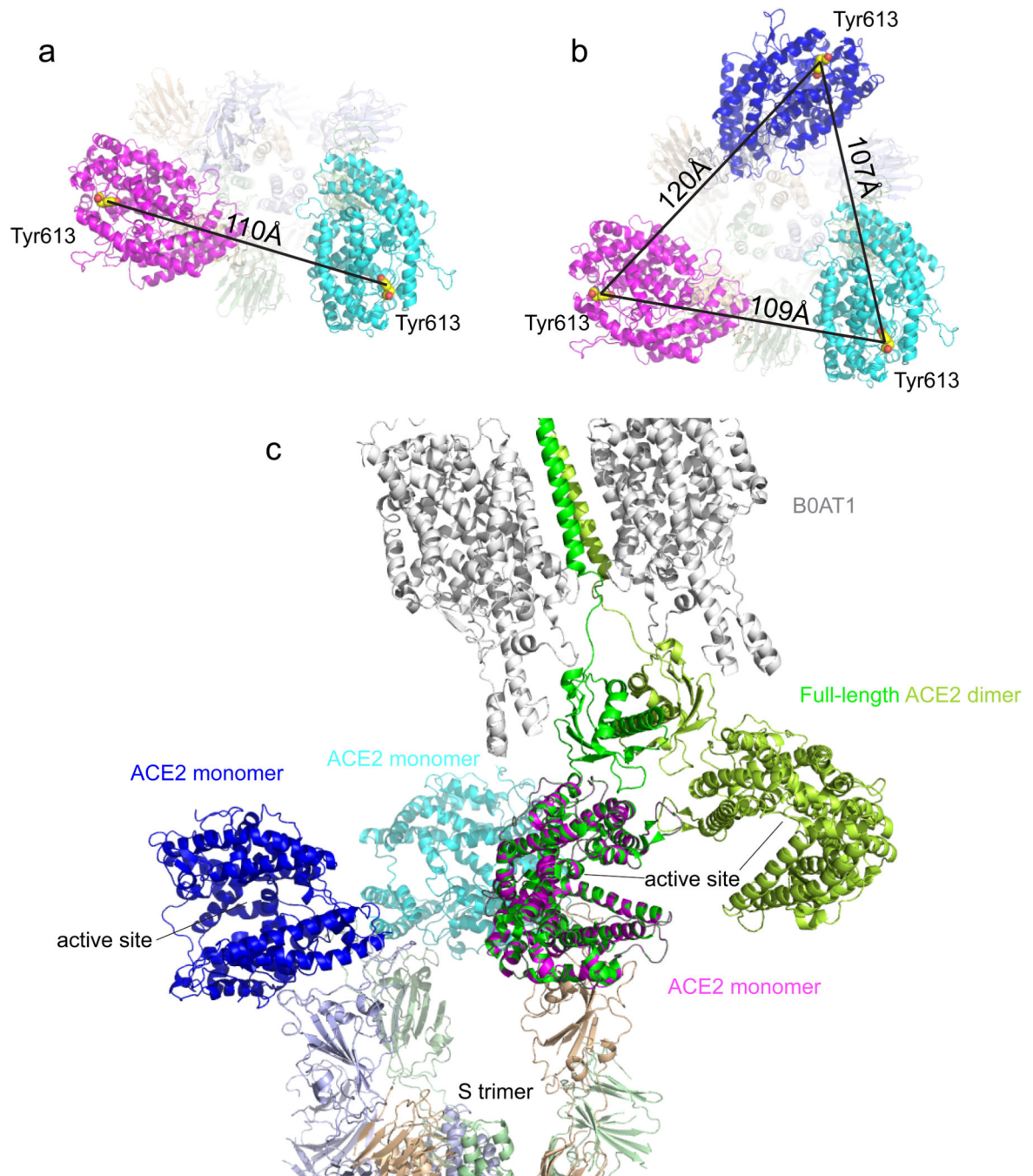
Extended Data Figure 4. ACE2-S interactions.
(a) The top view of the S trimer in complex with two monomeric ACE2 molecules (in magenta and cyan, respectively) with the distance between the C-terminal ends of the ACE2s indicated. (b) The top view of the S trimer in complex with three monomeric ACE2 molecules (in magenta, blue and cyan, respectively) with the distances between the C-terminal ends of the ACE2s indicated. (c) Superposition of the structure of the full-length ACE2 (PDB 6M17) and the structure of S-3 ACE2 complex.
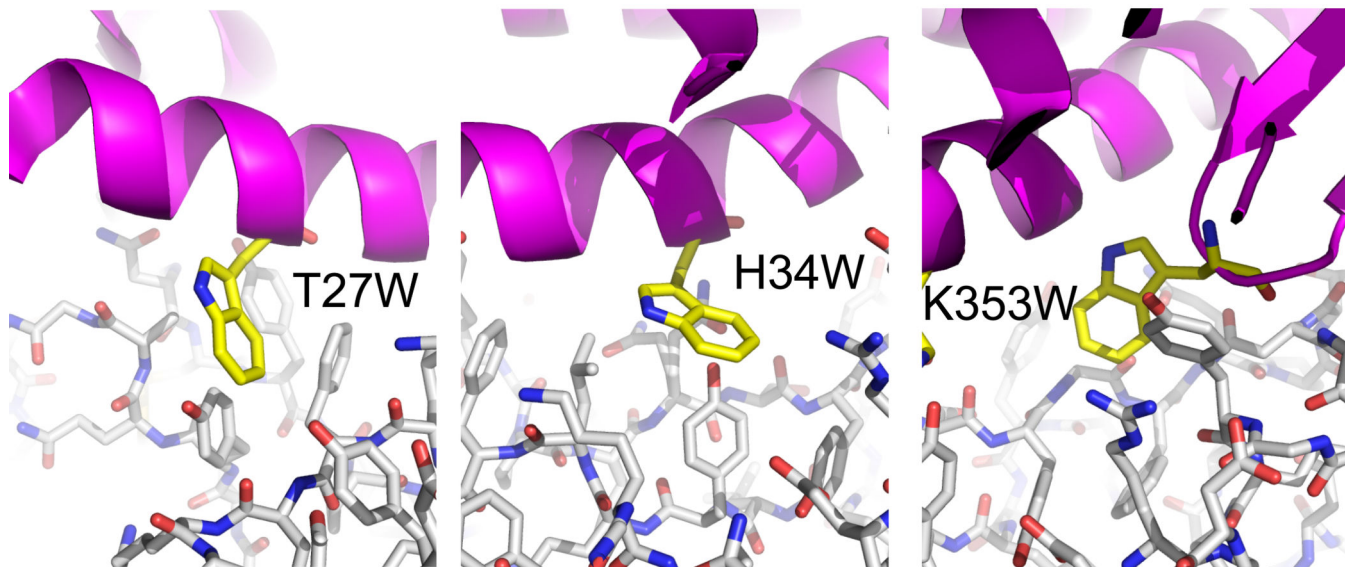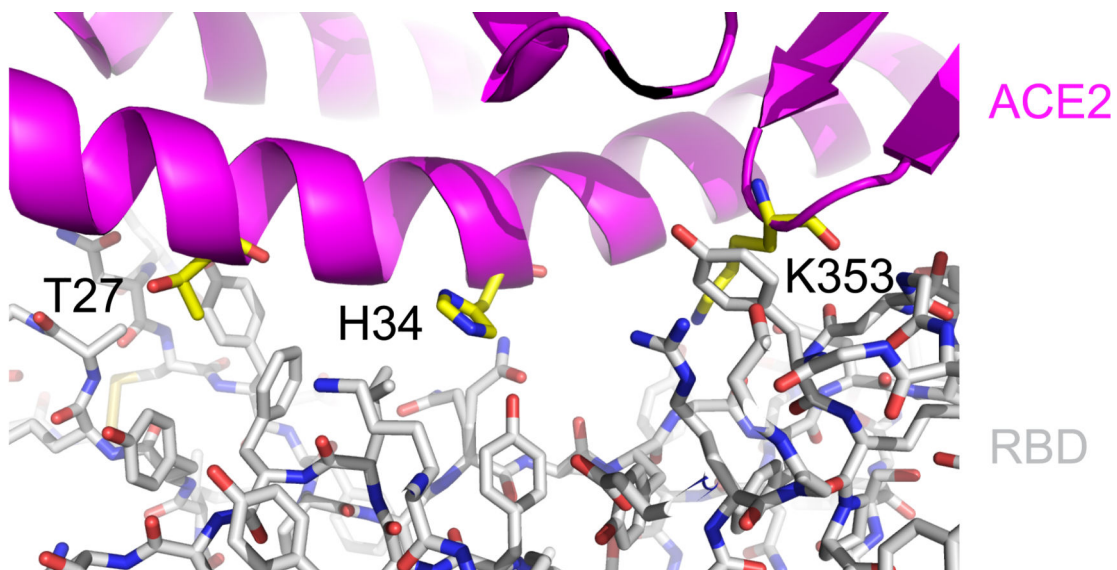
**Extended Data Figure 5. Design of mutations at the ACE2-RBD interface.**
Top, the interface between ACE2 in ribbon diagram in magenta and RBD in stick model from the complex structure (PDB 6M0J) with T27, H34 and K353 from ACE2 indicated. Bottom, modeled T27W, H34W and K353W mutations that may enhance the hydrophobic interactions between ACE2 and RBD.
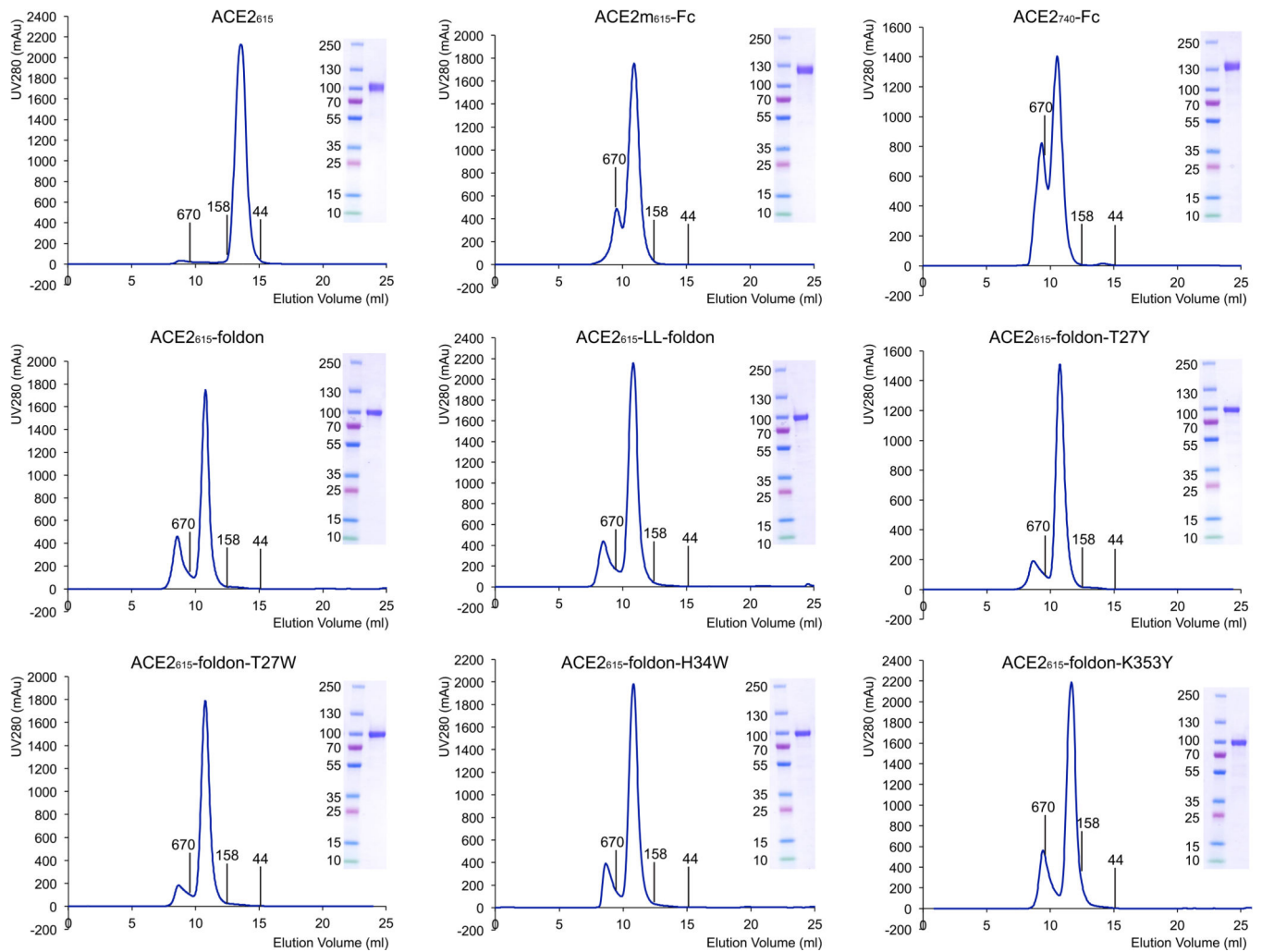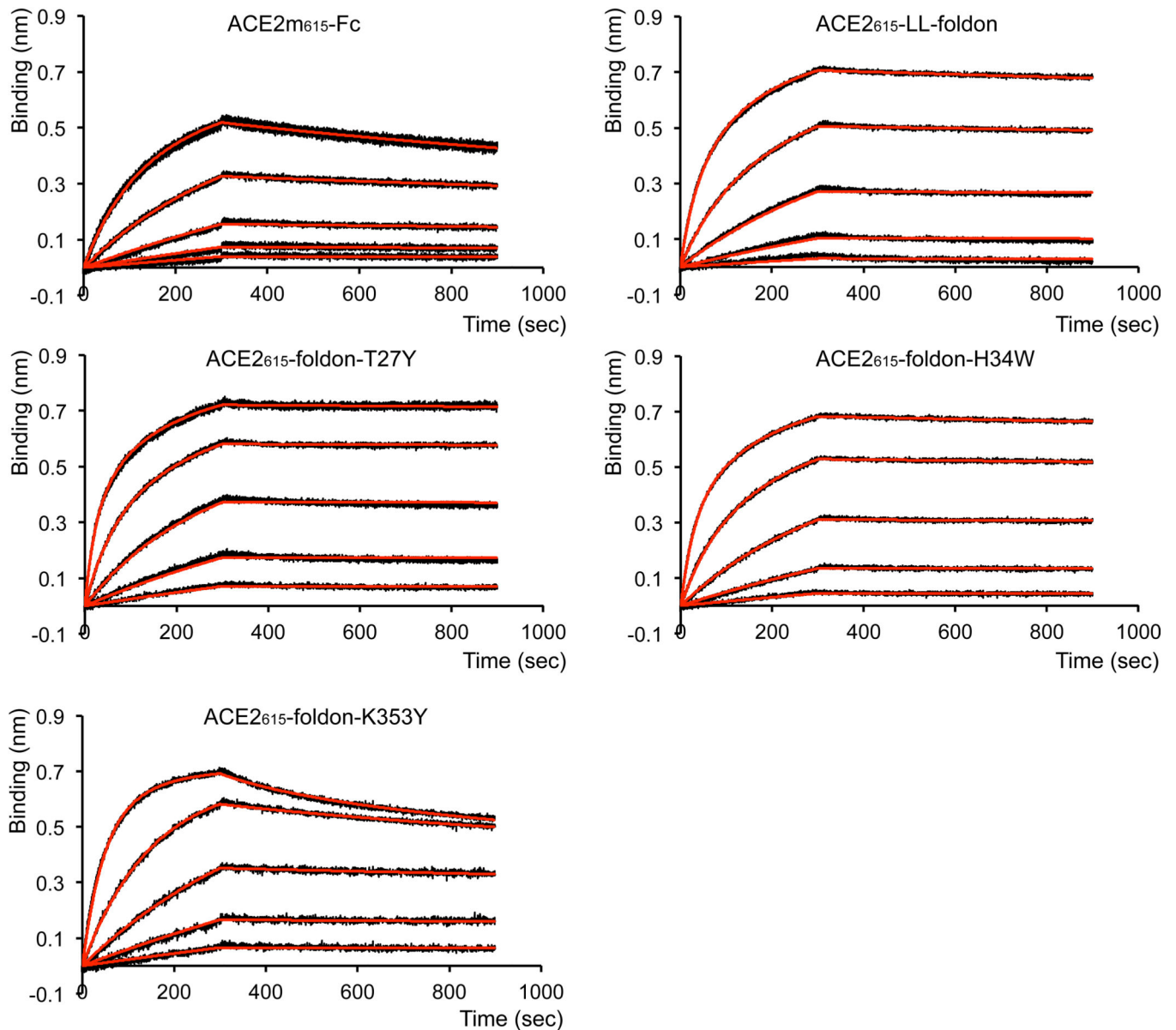
Extended Data Figure 6. Purification of ACE2 variants.
The purified ACE2 proteins were resolved by gel-filtration chromatography on a Superdex 200 column. The molecular weight standards include thyoglobulin (670 kDa), γ-globulin (158 kDa) and ovalbumin (44 kDa). Inset, peak fractions were analyzed by Coomassie stained SDS-PAGE. The uncropped image is available as source data.
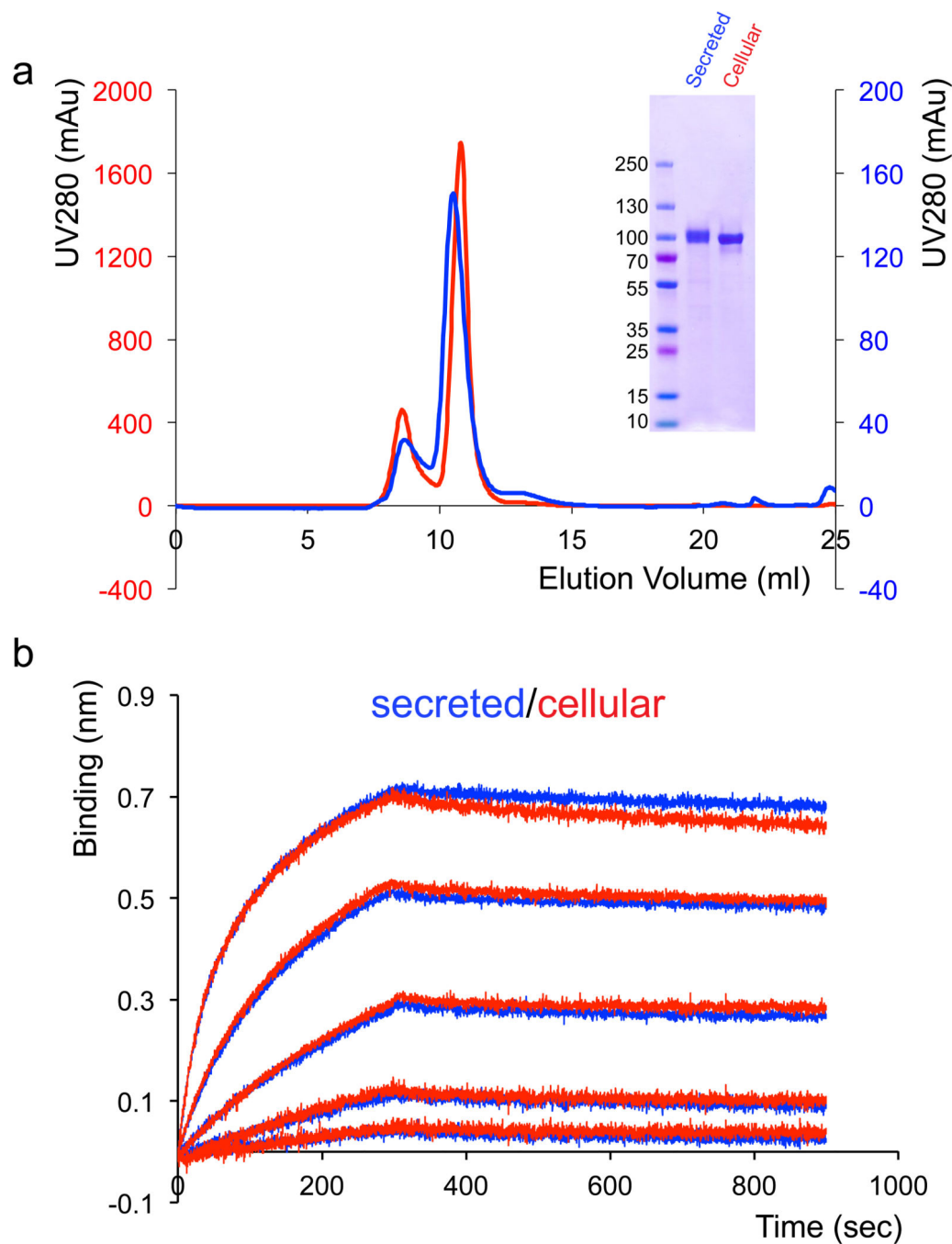
Extended Data Figure 7. Comparison of secreted and cellular ACE2$_{615}$-foldon protein.
(a) The purified ACE2$_{615}$-foldon protein either from cell supernatants (secrected) or cell lysates (cellular) was resolved by gel-filtration chromatography on a Superdex 200 column. Inset, peak fractions were analyzed by Coomassie stained SDS-PAGE. The uncropped image for panel a is available as source data. (b) Binding of ACE2$_{615}$-foldon to the stabilized soluble S trimer by bio-layer interferometry (BLI). The S protein was immobilized and subsequently dipped into the wells containing either secreted or cellular ACE2$_{615}$-foldon at

various concentrations (0.617–50 nM). The sensorgrams for the secreted ACE2$_{615}$-foldon are in blue and those for the cellular ACE2$_{615}$-foldon in red.

Extended Data Figure 8. Binding of ACE2 variants to the stabilized soluble S trimer by bio-layer interferometry (BLI).
The S protein was immobilized and subsequently dipped into the wells containing ACE2 proteins at various concentrations (0.926–75 nM for ACE2$_{615}$-Fc, 0.617–50 nM for the ACE2$_{615}$-foldon variants). Binding kinetics was evaluated using a bivalent model for all oligomeric ACE2s. The sensorgrams are in black and the fits in red. All the experiments were repeated at least twice with essentially identical results. Binding constants derived from the BLI experiments are summarized in Supplementary Table 3.

Supplementary Material

Refer to Web version on PubMed Central for supplementary material.

References:

1. Duan K et al. Effectiveness of convalescent plasma therapy in severe COVID-19 patients. Proc Natl Acad Sci U S A 117, 9490–9496 (2020). [PubMed: 32253318]

2. Bloch EM et al. Deployment of convalescent plasma for the prevention and treatment of COVID-19. J Clin Invest 130, 2757–2765 (2020). [PubMed: 32254064]

3. Shen C et al. Treatment of 5 Critically Ill Patients With COVID-19 With Convalescent Plasma. JAMA 323,1582–1589 (2020). [PubMed: 32219428]

4. Wec AZ et al. Broad neutralization of SARS-related viruses by human monoclonal antibodies. Science 369, 731–736 (2020). [PubMed: 32540900]

5. Shi R et al. A human neutralizing antibody targets the receptor binding site of SARS-CoV-2. Nature 584, 120–124 (2020). [PubMed: 32454512]

6. Chi X et al. A neutralizing human antibody binds to the N-terminal domain of the Spike protein of SARS-CoV-2. Science 369, 650–655 (2020). [PubMed: 32571838]

7. Wu Y et al. A noncompeting pair of human neutralizing antibodies block COVID-19 virus binding to its receptor ACE2. Science 368, 1274–1278 (2020). [PubMed: 32404477]

8. Xia S et al. Inhibition of SARS-CoV-2 (previously 2019-nCoV) infection by a highly potent pan-coronavirus fusion inhibitor targeting its spike protein that harbors a high capacity to mediate membrane fusion. Cell Res 30, 343–355 (2020). [PubMed: 32231345]

9. Xia S et al. Fusion mechanism of 2019-nCoV and fusion inhibitors targeting HR1 domain in spike protein. Cell Mol Immunol 17, 765–767 (2020). [PubMed: 32047258]

10. Sanders JM, Monogue ML, Jodlowski TZ & Cutrell JB Pharmacologic Treatments for Coronavirus Disease 2019 (COVID-19): A Review. JAMA 323,1824–1836 (2020). [PubMed: 32282022]

11. Wu R et al. An Update on Current Therapeutic Drugs Treating COVID-19. Curr Pharmacol Rep, 1–15, doi: 10.1007/s40495-020-00216-7 (2020).

12. Boulware DR et al. A Randomized Trial of Hydroxychloroquine as Postexposure Prophylaxis for Covid-19. N Engl J Med 383, 517–525 (2020). [PubMed: 32492293]

13. Jin Z et al. Structure of M(pro) from SARS-CoV-2 and discovery of its inhibitors. Nature 582, 289–293 (2020). [PubMed: 32272481]

14. Gao Y et al. Structure of the RNA-dependent RNA polymerase from COVID-19 virus. Science 368, 779–782 (2020). [PubMed: 32277040]

15. Polak SB, Van Gool IC, Cohen D, von der Thusen JH & van Paassen J A systematic review of pathological findings in COVID-19: a pathophysiological timeline and possible mechanisms of disease progression. Mod Pathol 33, 2128–2138 (2020). [PubMed: 32572155]

16. Zhou P et al. A pneumonia outbreak associated with a new coronavirus of probable bat origin. Nature 579, 270–273 (2020). [PubMed: 32015507]

17. Hoffmann M et al. SARS-CoV-2 Cell Entry Depends on ACE2 and TMPRSS2 and Is Blocked by a Clinically Proven Protease Inhibitor. Cell 181, 271–280 (2020). [PubMed: 32142651]

18. Lan J et al. Structure of the SARS-CoV-2 spike receptor-binding domain bound to the ACE2 receptor. Nature 581, 215–220 (2020). [PubMed: 32225176]

19. Shang J et al. Structural basis of receptor recognition by SARS-CoV-2. Nature 581, 221–224 (2020). [PubMed: 32225175]

20. Yan R et al. Structural basis for the recognition of SARS-CoV-2 by full-length human ACE2. Science 367, 1444–1448 (2020). [PubMed: 32132184]

21. Tikellis C, Bernardi S & Burns WC Angiotensin-converting enzyme 2 is a key modulator of the renin-angiotensin system in cardiovascular and renal disease. Curr Opin Nephrol Hypertens 20, 62–8 (2011). [PubMed: 21099686]

22. Clarke NE & Turner AJ Angiotensin-converting enzyme 2: the first decade. Int J Hypertens 2012, 307315 (2012).

23. Dasgupta C & Zhang L Angiotensin II receptors and drug discovery in cardiovascular disease. Drug Discov Today 16, 22–34 (2011). [PubMed: 21147255]

24. Hemnes AR et al. A potential therapeutic role for angiotensin-converting enzyme 2 in human pulmonary arterial hypertension. Eur Respir J 51, 1702638 (2018).

25. Imai Y et al. Angiotensin-converting enzyme 2 protects from severe acute lung failure. Nature 436, 112–6 (2005). [PubMed: 16001071]

26. Gu H et al. Angiotensin-converting enzyme 2 inhibits lung injury induced by respiratory syncytial virus. Sci Rep 6, 19840 (2016).

27. Zou Z et al. Angiotensin-converting enzyme 2 protects from lethal avian influenza A H5N1 infections. Nat Commun 5, 3594 (2014). [PubMed: 24800825]

28. Monteil V et al. Inhibition of SARS-CoV-2 Infections in Engineered Human Tissues Using Clinical-Grade Soluble Human ACE2. Cell 181, 905–913 e7 (2020). [PubMed: 32333836]

29. Kirchdoerfer RN et al. Stabilized coronavirus spikes are resistant to conformational changes induced by receptor recognition or proteolysis. Sci Rep 8, 15701 (2018).

30. Cai Y et al. Distinct conformational states of SARS-CoV-2 spike protein. Science 369, 1586–1592 (2020). [PubMed: 32694201]

31. Zhou T et al. A pH-dependent switch mediates conformational masking of SARS-CoV-2 spike. bioRxiv, doi: 10.1101/2020.07.04.187989 (2020).

32. Meier S, Guthe S, Kiefhaber T & Grzesiek S Foldon, the natural trimerization domain of T4 fibritin, dissociates into a monomeric A-state form containing a stable beta-hairpin: atomic details of trimer dissociation and local beta-hairpin stability from residual dipolar couplings. J Mol Biol 344, 1051–69 (2004). [PubMed: 15544812]

33. Korber B et al. Tracking Changes in SARS-CoV-2 Spike: Evidence that D614G Increases Infectivity of the COVID-19 Virus. Cell 182, 812–827 e19 (2020). [PubMed: 32697968]

34. Johnson MC et al. Optimized Pseudotyping Conditions for the SARS-COV-2 Spike Glycoprotein. J Virol 94, DOI: 10.1128/JVI.01062-20 (2020).

35. Haschke M et al. Pharmacokinetics and pharmacodynamics of recombinant human angiotensin-converting enzyme 2 in healthy human subjects. Clin Pharmacokinet 52, 783–92 (2013). [PubMed: 23681967]

36. Poglitsch M et al. Recombinant Expression and Characterization of Human and Murine ACE2: Species-Specific Activation of the Alternative Renin-Angiotensin-System. Int J Hypertens 2012, 428950 (2012).

37. Chan KK et al. Engineering human ACE2 to optimize binding to the spike protein of SARS coronavirus 2. Science 369, 1261–1265 (2020). [PubMed: 32753553]

38. Guo L et al. Engineered trimeric ACE2 binds viral spike protein and locks it in "Three-up" conformation to potently inhibit SARS-CoV-2 infection. Cell Res, 0,1–3; 10.1038/s41422-020-00438-w (2020). [PubMed: 31802008]

39. Cao L et al. De novo design of picomolar SARS-CoV-2 miniprotein inhibitors. Science 370, 426–431 (2020). [PubMed: 32907861]

40. Khan A et al. A pilot clinical trial of recombinant human angiotensin-converting enzyme 2 in acute respiratory distress syndrome. Crit Care 21, 234 (2017). [PubMed: 28877748]

41. Zoufaly A et al. Human recombinant soluble ACE2 in severe COVID-19. The Lancet. Respiratory Medicine, DOI:10.1016/S2213-2600(20)30418-5 (2020).

42. Barouch DH et al. Evaluation of a mosaic HIV-1 vaccine in a multicentre, randomised, double-blind, placebo-controlled, phase 1/2a clinical trial (APPROACH) and in rhesus monkeys (NHP 13–19). Lancet 392, 232–243 (2018). [PubMed: 30047376]

43. Mulligan MJ et al. Phase 1/2 study of COVID-19 RNA vaccine BNT162b1 in adults. Nature 586, 589–593 (2020). [PubMed: 32785213]

44. Sharma U et al. Structural basis of homo- and heterotrimerization of collagen I. Nat Commun 8, 14671 (2017).

45. Jevsevar S, Kunstelj M & Porekar VG PEGylation of therapeutic proteins. Biotechnol J 5, 113–28 (2010). [PubMed: 20069580]

46. Wrapp D et al. Cryo-EM structure of the 2019-nCoV spike in the prefusion conformation. Science 367, 1260–1263 (2020). [PubMed: 32075877]

47. Walls AC et al. Structure, function and antigenicity of the SARS-CoV-2 spike glycoprotein. Cell 181, 281–292 (2020). [PubMed: 32155444]

Methods-only References:

48. Zheng SQ et al. MotionCor2: anisotropic correction of beam-induced motion for improved cryo-electron microscopy. Nat Methods 14, 331–332 (2017). [PubMed: 28250466]

49. Rohou A & Grigorieff N CTFFIND4: Fast and accurate defocus estimation from electron micrographs. J Struct Biol 192, 216–21 (2015). [PubMed: 26278980]

50. Wagner T et al. SPHIRE-crYOLO is a fast and accurate fully automated particle picker for cryo-EM. Commun Biol 2, 218 (2019). [PubMed: 31240256]

51. Scheres SH RELION: implementation of a Bayesian approach to cryo-EM structure determination. J Struct Biol 180, 519–30 (2012). [PubMed: 23000701]

52. Emsley P, Lohkamp B, Scott WG & Cowtan K Features and development of Coot. Acta crystallographica. Section D, Biological crystallography 66, 486–501 (2010). [PubMed: 20383002]

53. Adams PD et al. PHENIX: a comprehensive Python-based system for macromolecular structure solution. Acta crystallographica. Section D, Biological crystallography 66, 213–21 (2010). [PubMed: 20124702]

54. Croll TI ISOLDE: a physically realistic environment for model building into low-resolution electron-density maps. Acta Crystallogr D Struct Biol 74, 519–530 (2018). [PubMed: 29872003]

55. Morin A et al. Collaboration gets the most out of software. Elife 2, e01456 (2013).

56. Millet JK & Whittaker GR Murine Leukemia Virus (MLV)-based Coronavirus Spike-pseudotyped Particle Production and Infection. Bio Protoc 6, e2035 (2016).

57. Chen CZ et al. Identifying SARS-CoV-2 entry inhibitors through drug repurposing screens of SARS-S and MERS-S pseudotyped particles. bioRxiv, doi: 10.1101/2020.07.10.197988 (2020)
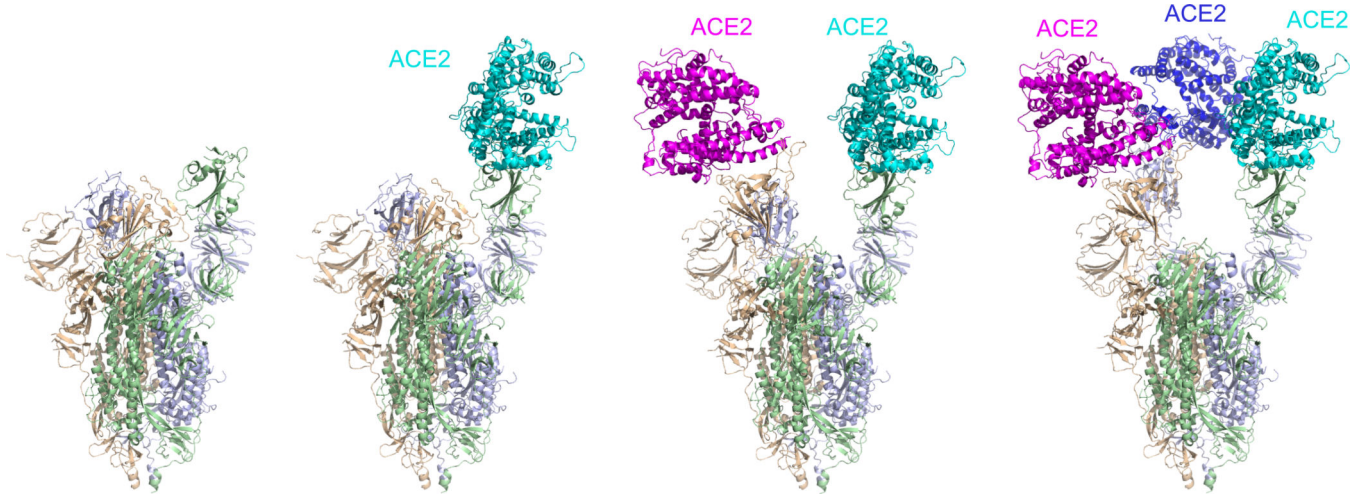
Figure 1. Cryo-EM structures of the ACE2-soluble S trimer complexes.
Four distinct classes were identified and refined from a sample prepared by mixing a monomeric ACE2 and the stabilized soluble SARS-CoV-2 trimer. Left, the structure of the S trimer without ACE2 in a conformation with one RBD up was modeled based on a 3.6-Å resolution density map. Three protomers are colored in green, blue and wheat, respectively. The structures of the S trimer in complex with one ACE2 (3.6Å), two ACE2 (3.7Å) or three ACE2 (3.4Å) are shown, with ACE2 colored in dark blue, cyan or magenta.
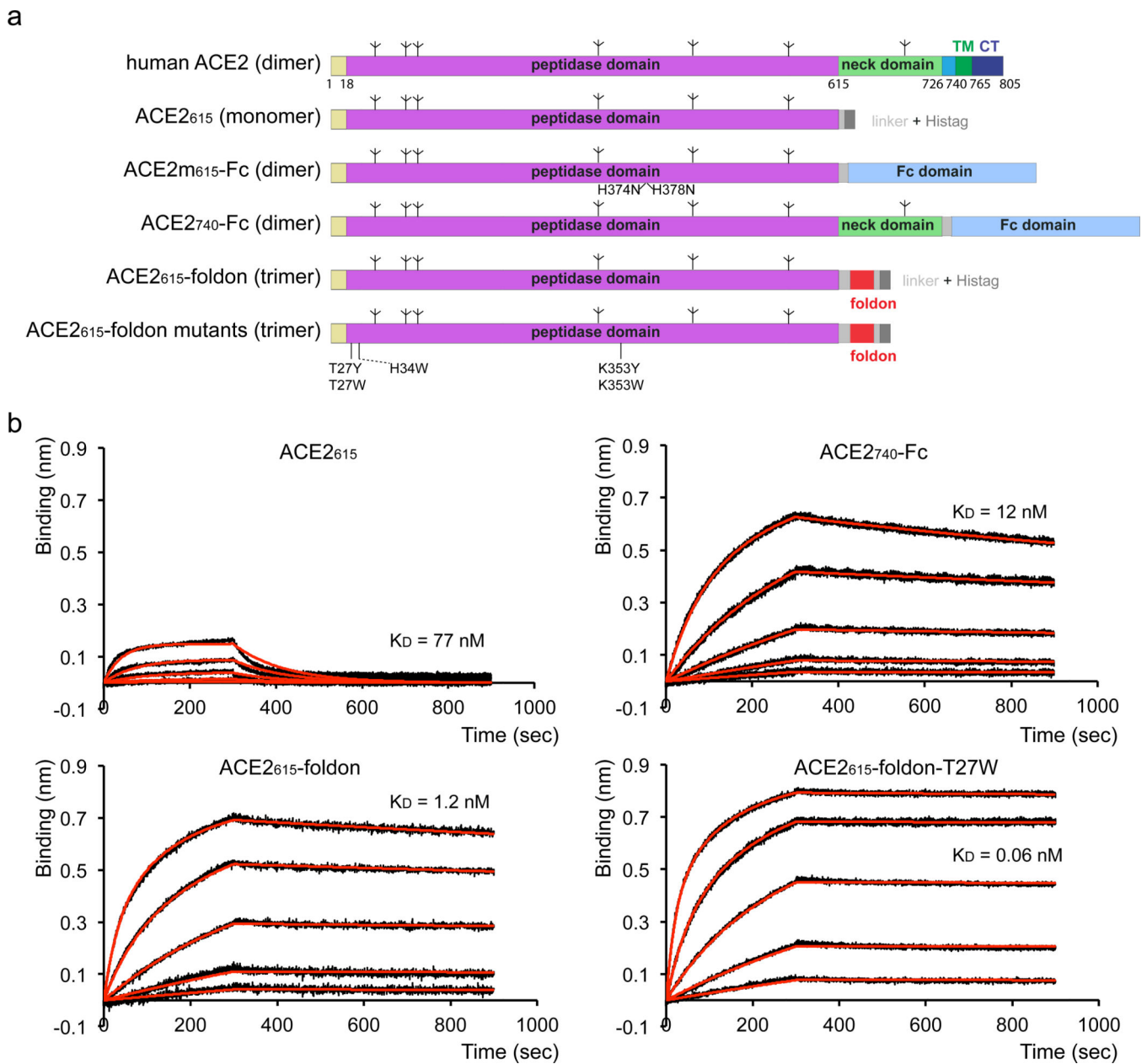
Figure 2. Design and characterization of ACE2 variants.

(a) Schematic representation of the full-length human ACE2. Various segments include: catalytic peptidase domain, neck domain; TM, transmembrane anchor; CT, cytoplasmic tail; tree-like symbols represent glycans. Expression constructs of various forms of ACE2 used in this study: ACE2$_{615}$, an inactive peptidase domain with mutations at the active site (H374N and H378N) fused with a C-terminal histag via a flexible linker; ACE2m$_{615}$-Fc, the peptidase domain fused to a Fc fragment of an immunoglobulin G at the C-terminus; ACE2$_{740}$-Fc, the peptidase and neck domains fused to a Fc fragment at the C-terminus; ACE2$_{615}$-foldon, the peptidase domain fused to a trimerization tag- foldon, followed by a C-terminal histag; ACE2$_{615}$-foldon mutants, single mutations (T27Y, T27W, H34W, K353Y and K353W) were introduced in the context of ACE2$_{615}$-foldon construct. (b) Binding of

ACE2 variants to the stabilized soluble S trimer by bio-layer interferometry (BLI). The S protein was immobilized to AR2G biosensors, which were dipped into the wells containing ACE2 at various concentrations (1.852–150 nM for $ACE2_{615}$, 0.926–75 nM for $ACE2_{740}$-Fc and 0.617–50 nM for all the $ACE2_{615}$-foldon variants). Binding kinetics was evaluated using a 1:1 Langmuir binding model for the monomeric $ACE2_{615}$ and a bivalent model for all other oligomeric ACE2. The sensorgrams are in black and the fits in red. All experiments were repeated at least twice with independent samples and essentially identical results. Binding constants derived from the BLI experiments are summarized in Table 2.
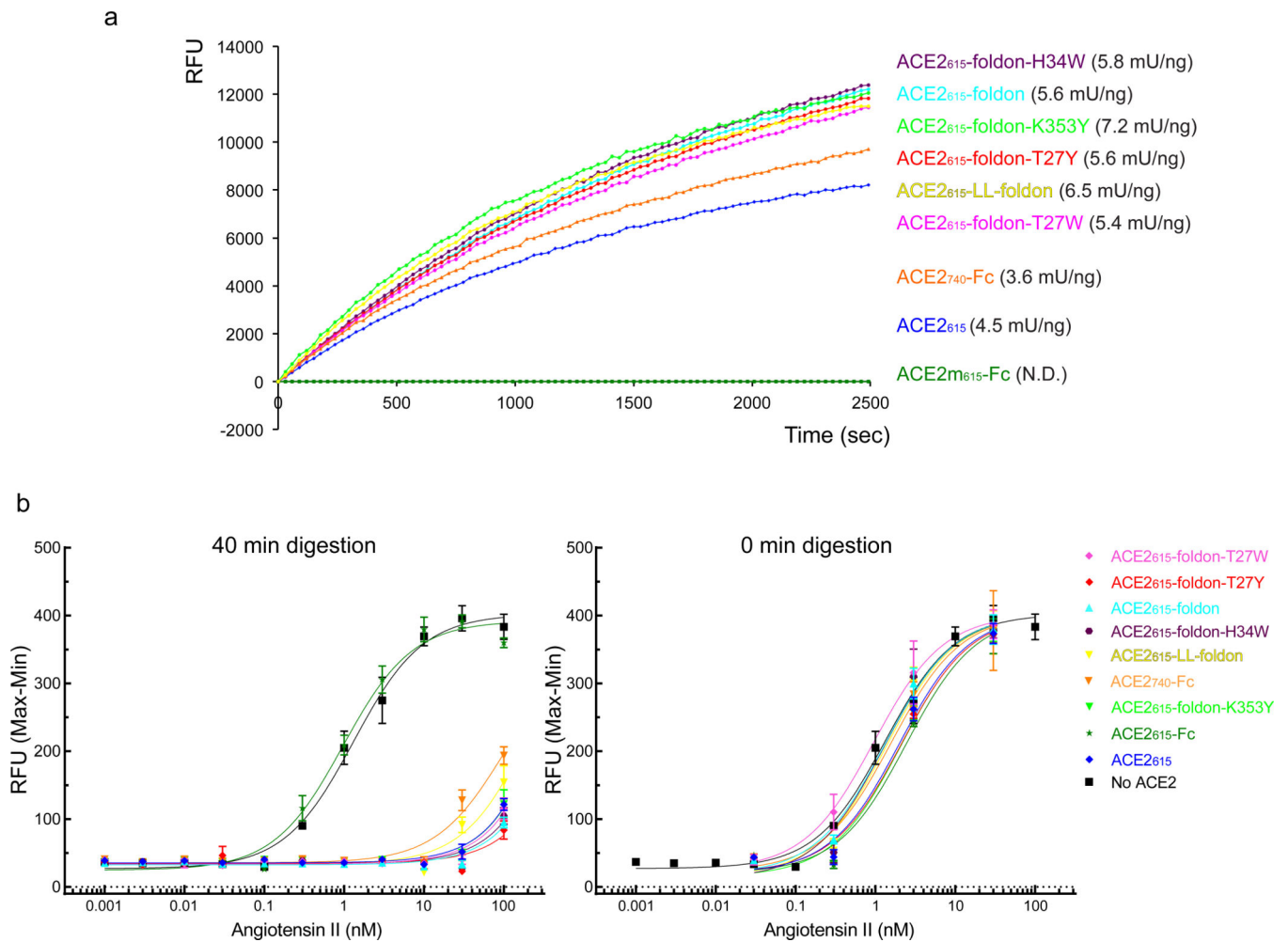
Figure 3. ACE2 peptidase activity and negative regulation of Ang II receptor type 1 activation.
(a) Peptidase activity of the ACE2 variants were measured by detecting free fluorophore released from a synthetic peptide substrate in a time-course experiment. Calculated specific activities are listed and summarized in Table 2. The experiment has been repeated twice with independent samples and similar results. (b) Ang II peptide was treated with various ACE2 variants before adding to the cells expressing Ang II receptor type 1 (AT1R) at different concentrations. AT1R activation was quantified by changes in the intracellular calcium concentration. Samples quenched at time 0 were used as controls. The y-axis is Ratio (Max-Min) (Peak fluorescent intensity - baseline fluorescent intensity). The EC_{50} values are summarized in Table 2. Data are mean and s.d. for $n = 4$ technical replicates; data behind graphs are available as source data. The experiment has been repeated at least three times with independent samples and similar results.
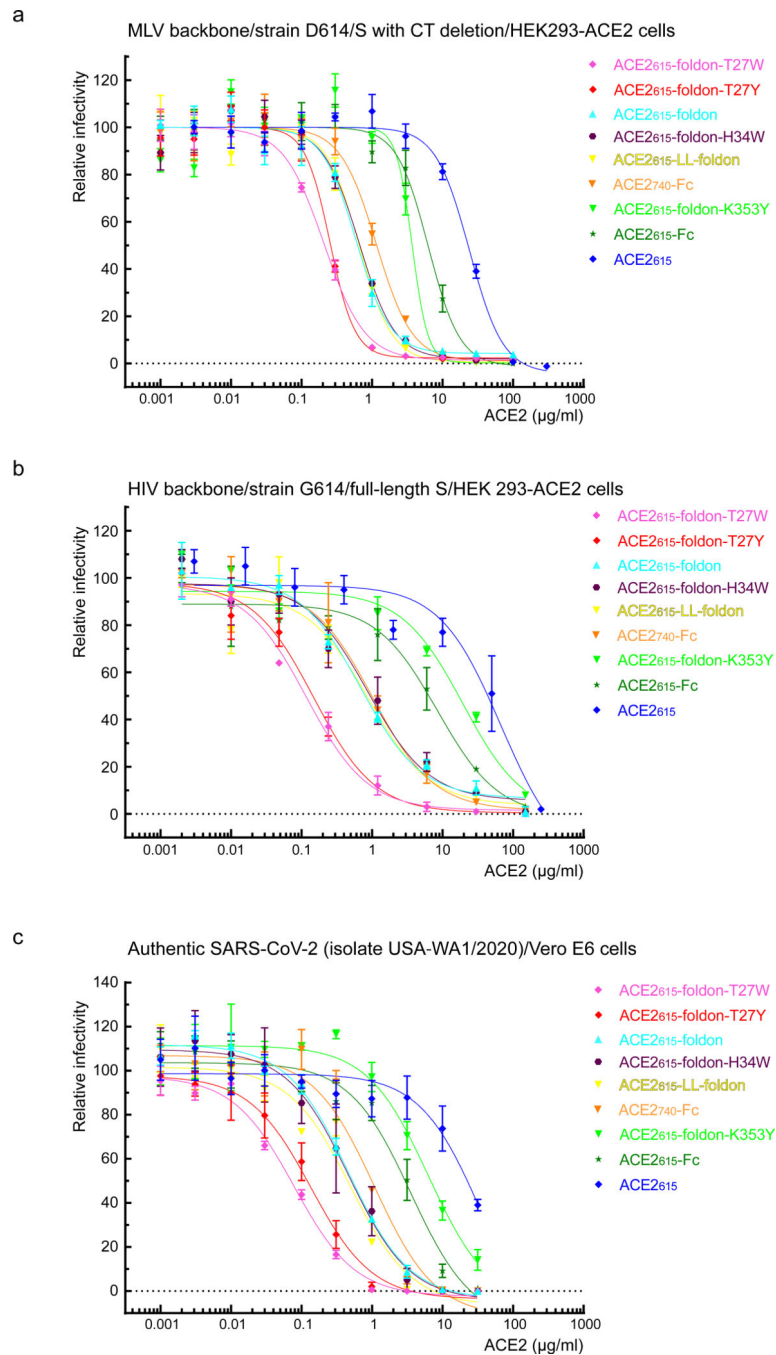
Figure 4. Inhibition of SARS-CoV-2 pseudoviruses and authentic viruses by ACE2 variants.
(a) Serial dilutions of each ACE2 variant were tested for inhibition against an MLV-based pseudotyped virus using a SARS-CoV-2 S construct containing D614 and a CT deletion in a single-round infection of HEK293-ACE2 cells. The experiments were repeated three times with independent samples giving similar results. (b) ACE2 variants were tested for inhibition against an HIV-based pseudotyped virus using a full-length SARS-CoV-2 S construct containing G614 in a single-round infection of HEK293-ACE2 cells. The experiments were repeated twice with independent samples giving similar results. (c) Serial dilutions of each

ACE2 variant were tested for inhibition against an authentic SARS-CoV-2 S virus (isolate USA-WA1/2020) infecting Vero E6 cells. The experiments were repeated three times with similar results. For all panels, data points shown are mean and s.d. for n = 3 technical replicates. Data behind graphs are available as source data. IC_{50} values derived from curve fitting are listed in Table 2 and Supplementary Table 2.

Table 1.

Cryo-EM data collection, refinement and validation statistics

	SARS-CoV-2 S (no ACE2) (EMD-22894, PDB 7KJ5)	SARS-CoV-2 S with 1 ACE2 (EMD-22891, PDB 7KJ2)	SARS-CoV-2 S with 2 ACE2 (EMD-22892, PDB 7KJ3)	SARS-CoV-2 S with 3 ACE2 (EMD-22893, PDB 7KJ4)
Data collection and processing				
Magnification			105,000	
Voltage (kV)			300	
Electron exposure (e$^-$/Å^2)			50.05	
Defocus range (μm)			1.6–2.7	
Pixel size (Å)			0.825	
Symmetry imposed			C1	
Initial particle images (no.)			407,761	
Final particle images (no.)	32,685	15,964	13,515	26,298
Map resolution (Å)	3.6	3.6	3.7	3.4
FSC threshold	0.143	0.143	0.143	0.143
Map resolution range (Å)	2.48–35.51	2.48–36.46	2.82–35.8	2.14–37.87
Refinement				
Initial model used (PDB ID)	6VYB	6VYB, 6M17	6VYB, 6M17	6VYB, 6M17
Model resolution (Å)	3.5	3.6	3.5	3.4
FSC threshold	0.5	0.5	0.5	0.5
Map sharpening B factor (Å^2)	-78.95	-83.01	-86.05	-74.38
Model composition				
Non-hydrogen atoms	23562	28560	33643	38776
Protein residues	2909	3502	4109	4722
Ligands	59	70	80	90
B factors (Å^2)				
Protein	46.79	57.46	65.84	185.79
Ligand	46.01	60.58	73.29	130.45
R.m.s. deviations				
Bond lengths (Å)	0.015	0.012	0.013	0.013
Bond angles (°)	1.997	1.857	1.826	1.900
Validation				
MolProbity score	2.02	1.99	1.95	1.96
Clashscore	5.44	6.69	6.29	4.77
Poor rotamers (%)	2.00	1.72	1.58	2.36
Ramachandran plot				
Favored (%)	91.62	93.12	92.84	93.40
Allowed (%)	7.95	6.38	6.46	6.09
Disallowed (%)	0.42	0.50	0.69	0.52

Table 2.

Binding affinity, peptidase function and SARS-CoV-2 inhibition potency of ACE2 constructs [a]

Construct	S Binding Affinity	Enzymatic Function			SARS-CoV-2 Inhibition Assay		
	K_D (nM)	specific activity (mU/ng)	EC_{50} (nM) at 0 min	EC_{50} (nM) at 40 min	IC_{50} (µg/ml) D614 pseudovirus	IC_{50} (µg/ml) G614 pseudovirus	IC_{50} (µg/ml) authentic virus
ACE2$_{615}$	76.8±0.8	4.54	2.0	N.D.	24.1	67.7	N.D.
ACE2m$_{615}$-Fc	22.3±2.2	N.D.	2.4	1.0	6.3	8.4	3.5
ACE2$_{740}$-Fc	12.4±0.6	3.59	1.6	N.D.	1.2	1.0	1.1
ACE2$_{615}$-Foldon	1.15±0.05	5.56	1.3	N.D.	0.59	0.69	0.46
ACE2$_{615}$-LL-Foldon	0.62±0.03	6.53	1.4	N.D.	0.65	0.90	0.49
ACE2$_{615}$-Foldon T27Y	0.09±0.01	5.56	2.1	N.D.	0.25	0.15	0.14
ACE2$_{615}$-Foldon T27W	0.06±0.01	5.41	1.0	N.D.	0.21	0.12	0.08
ACE2$_{615}$-Foldon H34W	0.37±0.01	5.75	1.3	N.D.	0.66	0.88	0.46
ACE2$_{615}$-Foldon K353Y	32.3±1.8	7.21	2.1	N.D.	3.7	19.5	6.3
No ACE2	N.A.	N.A.	1.3	1.3	N.A.	N.A.	N.A.

[a] Binding affinity measurements to SARS-CoV-2 soluble S trimer by bio-layer interferometry (BLI) shown in Fig. 2B and Extended Data Fig. 8 are summarized in column 2. Peptidase activities and measurements for inhibition of AT1R activation (Fig. 3) are listed in column 3–5. Negative regulation was indicated as activation by Ang II peptide after incubation with different ACE2 constructs for 40 min (EC50 at 40 min). Samples quenched at time 0 were used as controls, of which the Ang II activations (EC50 at 0 min) were summarized in column 4. Inhibition potency measurements in the assays using pseudoviruses and authentic viruses (Fig. 4) are listed in column 6–8.